Master thesis

Topological bands in cold gases

Sebastian Weber

November 3, 2015

University of Stuttgart
Institute for Theoretical Physics III

Supervised by
Prof. Dr. Hans Peter Büchler

Secondary corrector
Apl. Prof. Dr. Jörg Main

Declaration

I hereby declare that I wrote this master thesis on my own. To the best of my knowledge and belief, it contains no material previously published or written by another person, except where due acknowledgment has been made in the text.

Sebastian Weber

Stuttgart, November 3, 2015

Zusammenfassung

In der Festkörperphysik gibt es sehr spannende und zum Teil noch nicht vollständig verstandene Phänomene wie den fraktionalen Quanten-Hall-Effekt [1, 2], die in zweidimensionalen Systemen mit topologischen Bandstrukturen auftreten [3, 4]. „Topologisch“ bedeutet hier, dass die Bänder eine Chern-Zahl ungleich Null haben. Bei dieser Zahl handelt es sich um eine topologische Invariante. Ein bekanntes Beispiel für solch eine Invariante ist das topologische Geschlecht, also die Anzahl der Löcher in einer orientierbaren Fläche (zum Beispiel Null bei einer Kugeloberfläche und Eins bei einer Torusoberfläche). Nur unstetige Transformationen können topologische Invarianten ändern. Daher ist die Chern-Zahl stabil, solange sich keine Bandlücken schließen. Dies hat interessante Phänomene wie quantenmechanische Randzustände und einen quantisieren Hall-Widerstand [5] zufolge.

In der vorliegenden Arbeit geht es darum, wie man mit Hilfe von dipolarer Wechselwirkung topologische Bänder erzeugen kann. Die vor kurzem vorgestellte Grundidee [6] ist, dass die Spin-Bahn-Kopplung der dipolaren Wechselwirkung eine atomare Anregung hüpfen und eine komplexe Phase aufsammeln lässt. Bei gebrochener Zeitumkehrsymmetrie [7] lassen sich hierdurch topologische Bänder realisieren. In dieser Arbeit zeigen wir detailliert, wie dies mit Rydbergatomen (also Atomen mit einem hoch angeregten Elektron) gemacht werden kann. Rydbergatome eignen sich besonders gut wegen ihrer starken dipolaren Wechselwirkung und der guten Manipulierbarkeit ihrer Energieniveaus mit elektromagnetischen Feldern. Da uns die experimentelle Realisierbarkeit wichtig ist, legen wir unseren Fokus auf möglichst kleine, einfache Systeme. Um diese besser analysieren zu können, entwickeln wir eine Art Bandstruktur, die auch für endliche Systeme berechnet werden kann. Wir zeigen ein System mit zehn Atomen, in dem experimentell gut zu untersuchende Randzustände als Überbleibsel topologischer Bänder zu finden sind. Nützlich für die experimentelle Realisierung ist auch die Robustheit der Systeme — die optischen Gitter, in denen sich die Atome befinden, müssen daher nicht perfekt sein. Wenn wir die Wechselwirkung auf kleinen Längenskalen zum Beispiel mit der Rydbergblockade unterdrücken, werden die Systeme unseren Berechnungen zufolge sogar noch robuster. Außerdem nähern wir uns hierdurch einem von uns entdeckten Kontinuumsmodell an, dessen Eigenschaften analytisch bestimmt werden können. Dies zeigt, dass auch andere Phänomene als der Quanten-Hall-Effekt topologische Bänder im Kontinuum hervorbringen können.

Unser Plan für die Zukunft ist, in den untersuchten Systemen die Vielteilchengrundzustände mittels exakter Diagonalisierung zu analysieren. Wir hoffen, Phänomene ähnlich des fraktionalen Quanten-Hall-Effekts zu entdecken.

Abstract

In the world of solid state physics, there are interesting, yet not fully understood phenomena like the fractional quantum Hall effect [1, 2] that rely on topological band structures. Here, the term “topological” means that the bands have a non-vanishing topological invariant called Chern number [3, 4]. A well-known example of a topological invariant in the fields of mathematics is the genus that is the number of handles of an orientable surface (for example, the surface of a sphere has a genus of zero whereas the surface of a torus has a genus of one). A topological invariant can only change under non-continuous deformations. Thus, the Chern number is stable as long as there are no band closings. This result can explain interesting phenomena like edge states and the quantized Hall conductivity [5].

The thesis deals with the realization of topological bands in two-dimensional cold gases setups via dipolar interaction. The key idea was developed recently [6] and is based on the following observation: The spin-orbit coupling of the dipolar interaction makes atomic excitations hop with complex tunneling amplitudes, so that they collect a phase. In case of broken time reversal symmetry [7], this can lead to topological bands. In this thesis, we show a detailed and realistic experimental proposal on how we can implement this idea using Rydberg atoms (e.g. atoms with one highly excited electron). Rydberg atoms are well suited because of their strong dipolar interaction and the ability to easily tune their level structures through static electromagnetic fields. Since the experimental feasibility is important to us, we focus on small systems. In order to analyze them in detail, we develop a band structure analogue, that can tell us the dispersion of edge states in finite systems and their number. We achieve a system with as few as ten Rydberg atoms that still shows edge states as remnants of topological bands. The robustness of edge states allows the realization of interesting systems in optical lattices with slight imperfections. We can increase the robustness to lattice defects even more if we use cutoff potentials that suppress the interaction on small length scales. Furthermore, these potentials give rise to a continuum-like model, whose properties can be calculated analytically. This shows that there are phenomena other than the quantum Hall effect that can lead to topological bands in the continuum as well.

Our plan for the future is to search for many-body effects in these systems via exact diagonalization. We hope to find phenomena similar to the fractional quantum Hall effect.

Contents

Introduction

Since the discovery of the integer quantum Hall effect (QHE) in 1980 [5], many related systems were found. It was shown that QHE-like phenomena neither rely on free electrons nor on net magnetic fields. For example, the Haldane model [8] shows edge states and a quantized Hall resistance although there is no net magnetic field and the electrons are in a lattice. Despite their differences, these systems have in common that moving particles collect complex phases in such a way that the band structures get topological, i.e. bands have non-zero Chern numbers[1] [3, 4]. In systems with boundaries, this gives rise to edge states that are the reason for the quantized Hall conductivity of topological bands that are fully filled with weakly interacting fermions. Fractionally filled topological bands are the basis of the fractional QHE (for strongly interacting electrons) [1, 2] and the fractional topological insulator (for strongly interacting particles in a lattice) [9]. Both systems are not fully understood[2] and the latter has not been experimentally realized, yet. Furthermore, phenomena originating from topological bands are of practical relevance: The integer QHE is used as an electrical resistance standard [10] and fractional states might be suitable for topological quantum computing [11].

For these reasons, major effort is put in the development of systems with topological bands. Many proposals and experimental realizations rely on well controllable cold gases setups: Shaken optical lattices [12, 13] or Raman-assisted tunneling [14–16] make atoms or excitations hop with complex tunneling amplitudes. Both approaches generate artificial gauge fields that emulate (staggered) magnetic fields. However, since lattice shaking and AC fields cause possible heating, fractional topological insulators might be hard to realize with these techniques.

In this thesis, we deal with a different method for the realization of topological bands with cold gases. The recently developed approach [6], that we are going to use, relies on spin-orbit coupling by dipolar interaction [17] and does not have the drawback of possible heating. Other interesting features of this dipolar model are the intrinsic long-range tunneling and the dependence of the collected phase on enclosed angles instead areas. Hence, it is fundamentally different to artificial gauge fields.

The goal of the thesis is to develop a realistic experimental proposal for topological bands based on this dipolar model and to investigate whether it give rise to new, interesting

---

[1] The Chern number is the topological invariant of bands (analogues to the genus that is the topological invariant of orientable surfaces). As such, the Chern number can not change under adiabatic deformations of bands. It is stable unless a band gap closes.

[2] For example, it is still not known what explains the existence of the $v = 5/2$ fractional quantum Hall state.

phenomena. The thesis consists of four parts: In chapter 1 we introduce fundamental concepts like the Chern number and describe the dipolar model [6] in detail. After this introduction of theoretical essentials, we develop a band structure analogue for finite systems in chapter 2, so that we can determine the dispersion of edge states in small systems and their number. In chapter 3, we make use of the band structure analogue to develop a realistic proposal for topological bands using Rydberg atoms in a deep, two-dimensional optical lattice. In chapter 4, we apply cutoff potentials to make topological bands more robust to lattice defects. In addition, our cutoff potentials lead to a continuum model that we investigate in this chapter as well. It shows that topological bands in the continuum can originate from other phenomena than the QHE, too.

1. Theoretical basis

1.1. Chern number

Topological invariants are properties of a “geometric object” that are invariant under continuous deformations. Hence, they are robust to small perturbations. A well known example is the genus, which is the number of handles of an orientable surface.

In case of band structures, we can calculate the Chern number C_n. It is the topological invariant of the n-th band in a gapped system. Here, “invariant under continuous deformations” means “invariant under adiabatic transformations of bands”. This implies that the Chern number can only change if a band gap closes. The Chern number is related to the Hall conductivity σ_{xy} via[1]

$$\sigma_{xy} = \frac{e^2}{h} \sum_{\text{filled bands}} C_n. \tag{1.1}$$

If the Chern number is non-zero, we call a band topological. Topological bands are the basis for interesting phenomena like the (fractional) quantum Hall effect and (fractional) topological Chern insulators.

The Chern number can be calculated from the eigenstates that belong to a band. It is proportional to the Berry curvature $\boldsymbol{\Omega}$ integrated over the whole Brillouin zone as it is demonstrated e.g. in the chapters 2, 3, and 8 of the book “Topological Insulators and Topological Superconductors” by B. A. Bernevig [18]:

$$C_n = -\frac{1}{2\pi} \mathrm{Im} \int_{BZ} \mathrm{d}\boldsymbol{S} \cdot \boldsymbol{\Omega}(\boldsymbol{k}). \tag{1.2}$$

The Berry curvature is given by

$$\boldsymbol{\Omega}_\alpha(\boldsymbol{k}) = \epsilon_{\alpha\beta\gamma} \langle \nabla_\beta n(\boldsymbol{k}) | \nabla_\gamma n(\boldsymbol{k}) \rangle, \text{ where } |n(\boldsymbol{k})\rangle \text{ are the eigenstates of the band } n. \tag{1.3}$$

Unfortunately this formula contains derivatives of eigenstates, what will cause problems: In numerical calculations, the eigenstates are usually calculated independently for each $\boldsymbol{k}$ and hence have different global phase factors. We would have to gauge-smooth first, before we would be able to calculate the derivatives. In order to circumvent this issue we rewrite the equation for the Berry curvature as it is shown in [18].

---

[1] We use the same sign conventions as [3] for the Chern number and the Hall conductivity. In [4, 18] different sign conventions are used.

For this purpose we insert the sum $\sum_m |m\rangle\langle m|$ over all eigenstates into 1.3. That gives us

$$\boldsymbol{\Omega}_\alpha(\boldsymbol{k}) = \sum_m \epsilon_{\alpha\beta\gamma}\langle\nabla_\beta n(\boldsymbol{k})|m(\boldsymbol{k})\rangle\langle m(\boldsymbol{k})|\nabla_\gamma n(\boldsymbol{k})\rangle. \tag{1.4}$$

Since we have $\langle n|n\rangle = 1$, the equation $\nabla\langle n|n\rangle = \langle n|\nabla n\rangle + \langle n|\nabla n\rangle^* = 0$ holds. Thus, $\langle\nabla_\beta n(\boldsymbol{k})|n(\boldsymbol{k})\rangle\langle n(\boldsymbol{k})|\nabla_\gamma n(\boldsymbol{k})\rangle$ is a product of two imaginary numbers and hence real. Therefore we can neglect this term from the sum 1.4 because only imaginary numbers contribute to the Chern number 1.2.

Finally, we would like to remove the derivatives on the eigenstates using $E_n\langle m|\nabla n\rangle = \langle m|\nabla(Hn)\rangle = \langle m|(\nabla H)|n\rangle + E_m\langle m|\nabla n\rangle$, this implies

$$\langle m|\nabla n\rangle = \frac{\langle m|(\nabla H)|n\rangle}{E_n - E_m}. \tag{1.5}$$

Doing so, we obtain the following formula for the Chern number:

$$C_n = -\frac{1}{2\pi}\mathrm{Im}\int_{BZ} \mathrm{d}\boldsymbol{S}_\alpha \cdot \sum_{m\neq n} \epsilon_{\alpha\beta\gamma}\frac{\langle n(\boldsymbol{k})|(\nabla_\beta H)|m(\boldsymbol{k})\rangle\langle m(\boldsymbol{k})|(\nabla_\gamma H)|n(\boldsymbol{k})\rangle}{(E_n(\boldsymbol{k}) - E_m(\boldsymbol{k}))^2}. \tag{1.6}$$

In our case, the Brillouin zone lies in the XY-plane. This simplifies the equation to

$$C_n = -\frac{1}{2\pi}\mathrm{Im}\int_{BZ} \mathrm{d}^2\boldsymbol{k} \sum_{m\neq n} \frac{\langle n(\boldsymbol{k})|(\nabla_x H)|m(\boldsymbol{k})\rangle\langle m(\boldsymbol{k})|(\nabla_y H)|n(\boldsymbol{k})\rangle - (x \leftrightarrow y)}{(E_n(\boldsymbol{k}) - E_m(\boldsymbol{k}))^2}. \tag{1.7}$$

We will use this formula to calculate Chern numbers numerically. Besides, the equation leads to the final conclusion that the Chern numbers of all bands sum up to zero.

1.1.1. Formula for systems with two bands

The Hamiltonian of a system with two bands can always be expressed in terms of Pauli matrices. It can be written as

$$H = \sum_{\boldsymbol{k}} \boldsymbol{\psi}^\dagger_{\boldsymbol{k}} \left(c_{\boldsymbol{k}}\mathbb{1} + \boldsymbol{n}_{\boldsymbol{k}}\cdot\boldsymbol{\sigma}\right) \boldsymbol{\psi}_{\boldsymbol{k}} \tag{1.8}$$

with $c_{\boldsymbol{k}} = \frac{1}{2}\mathrm{tr}(H)$ and $\boldsymbol{n}_{\boldsymbol{k}} = \frac{1}{2}\mathrm{tr}(H\boldsymbol{\sigma})$, where $\boldsymbol{\sigma}$ is the vector of Pauli matrices. Then, we can calculate the Chern number as the winding number of the normalized vector $\hat{\boldsymbol{n}}_{\boldsymbol{k}} = \boldsymbol{n}_{\boldsymbol{k}}/|\boldsymbol{n}_{\boldsymbol{k}}|$ — like it is done in [6] — via [18]

$$C = \frac{1}{4\pi}\int_{BZ} \mathrm{d}^2\boldsymbol{k}\ (\partial_{k_x}\hat{\boldsymbol{n}}_{\boldsymbol{k}} \times \partial_{k_y}\hat{\boldsymbol{n}}_{\boldsymbol{k}})\cdot\hat{\boldsymbol{n}}_{\boldsymbol{k}} \tag{1.9}$$

The fact, that the Chern number is a winding number, directly shows us that it is integer-valued. This also implies the previously mentioned theorem that the Chern number can not change if bands deform adiabatically, i.e. if there is no band closing.

1.1.2. Bulk edge correspondence

The number of edge states is determined by the difference in the Chern numbers [3].

This statement can be intuitively understood if one considers a half-finite system that implements a model with two topological bands. At the boundaries of the system the Chern numbers has to change to the Chern number of the vacuum, which is zero. For it the band gap has to close. This implies the existence of "edge bands", commonly called edge states, that bridge the band gap. Rigorous proofs of the bulk edge correspondence are difficult [19, 20].

1.2. Haldane model

A renowned model featuring topological bands is the Haldane model [8]. It is a model on a honeycomb lattice with a staggered magnetic field as it is shown in figure 1.1. Nearest and next-nearest neighbor tunneling of electrons is considered.

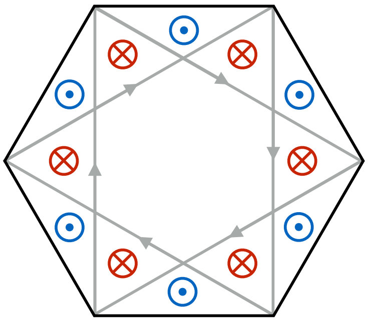

Fig. 1.1.: Unit cell of the Haldane model. A phase equal to ϕ is collected along the arrows due to the staggered magnetic field. In the opposite direction, the collected phase is $-\phi$.

The field is chosen in such a way that there is no net magnetic field in the unit cell. Nevertheless the staggered magnetic field gives rise to topological bands by creating complex next-nearest neighbor tunneling amplitudes. The nearest neighbor tunneling is chosen to be real. The Hamiltonian of the system is given by

$$H = t_1 \sum_{\langle i,j \rangle} c_i^\dagger c_j + t_2 \sum_{\langle\langle i,j \rangle\rangle} \mathrm{e}^{\mathrm{i}\nu_{ij}\phi}\, c_i^\dagger c_j + \mu \sum_{i \in A} c_i^\dagger c_i - \mu \sum_{i \in B} c_i^\dagger c_i, \tag{1.10}$$

where ν_{ij} is $+1$ if the electrons hops in the direction of the arrows in figure 1.1 and -1 otherwise. The complex tunneling ϕ breaks time-reversal symmetry. The energy difference 2μ between the two sublattices A and B breaks inversion symmetry. Depending on the value of the parameters the model is topologically trivial or has bands with a Chern number of ± 1. The topological phase diagram is shown in figure 1.2.

We will use this well-known model in chapter 2 for the demonstration of a novel band structure analog for finite systems.

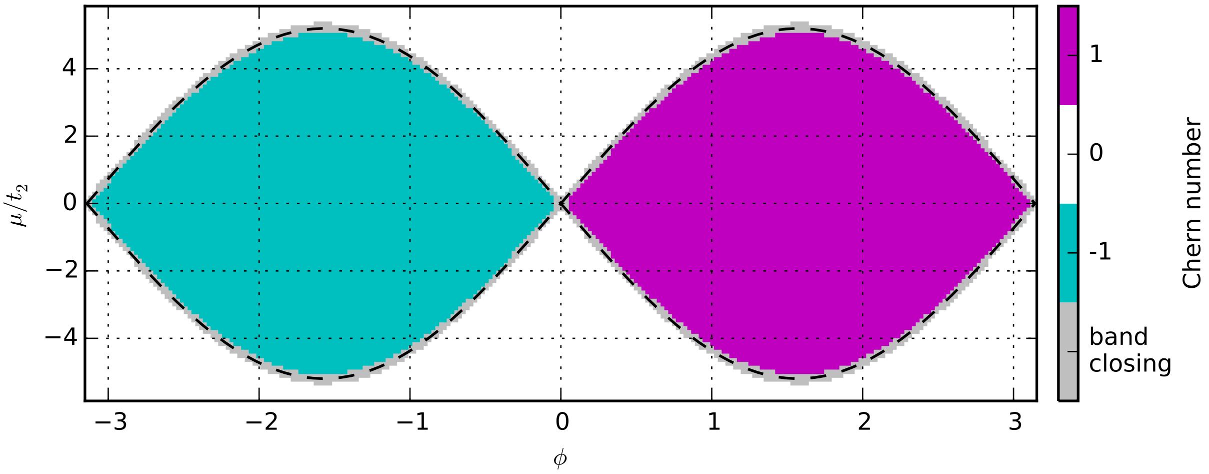

Fig. 1.2.: Topological phase diagram of the Haldane model. We calculated it numerically as a test case for our software. The dotted lines show the analytic solutions for the phase boundaries [8].

1.3. Topological bands from dipolar interaction

In the remaining chapters of the thesis we devote ourselves to a model that was proposed in [6]. One can make use of dipolar interaction to create topological bands. The idea is to place particles with a strong dipolar interaction into a two-dimensional lattice. Assuming that they obey a level structure like it is shown in figure 1.3, the dipolar interaction let an excitation to the $|+\rangle$ or $|-\rangle$ orbital hop with complex tunneling amplitudes through spin-orbit coupling.

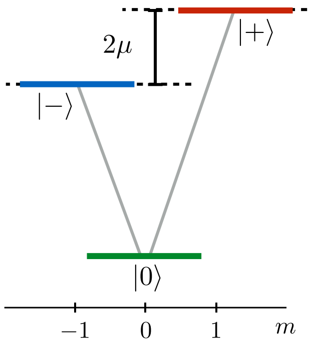

Fig. 1.3.: Level structure of the particles whose dipolar interaction gives rise to topological bands.

This can be directly seen from the dipolar interaction operator

$$\hat{V}_{ij}^{\mathrm{dd}} = \frac{1}{4\pi\epsilon_0|\boldsymbol{R}_{ij}|^3}\left[d_i^0 d_j^0 + \frac{1}{2}\left(d_i^+ d_j^- + d_i^- d_j^+\right) - \frac{3}{2}\left(d_i^- d_j^- \mathrm{e}^{2\mathrm{i}\phi_{ij}} + d_i^+ d_j^+ \mathrm{e}^{-2\mathrm{i}\phi_{ij}}\right)\right], \quad (1.11)$$

that is derived in appendix E. Because we have no levels that can be coupled with d^0, we are allowed to neglect the first summand $d_i^0 d_j^0$. The factor 2 in the exponent of the complex tunneling amplitude can be understood as a consequence of angular momentum conservation since it is connected to a spin-flip hopping process where the excitation changes from $|+\rangle$ at site j to $|-\rangle$ at site i. Furthermore, the phase of the complex tunneling[2] depends on the hopping angle $\phi_{ij} = \angle(\boldsymbol{R}_j - \boldsymbol{R}_i)$, see figure E.1.

The excitations $|\pm\rangle_i$ can be interpreted as hard-core bosons. Using the definitions $b^\dagger_{i,\pm} = |\pm\rangle_i\langle 0|_i$ and $\boldsymbol{\psi}^\dagger_i = (b^\dagger_{i,+}, b^\dagger_{i,-})$ we can rewrite the interaction operator as

$$\hat{V}^{\text{dd}}_{ij} = \frac{a^3}{|\boldsymbol{R}_{ij}|^3}\boldsymbol{\psi}^\dagger_i \begin{pmatrix} -t_+ & w\mathrm{e}^{-2\mathrm{i}\phi_{ij}} \\ w\mathrm{e}^{2\mathrm{i}\phi_{ij}} & -t_- \end{pmatrix} \boldsymbol{\psi}_j + \text{h.c.}, \tag{1.12}$$

like it is done in [6]. Here, a is the lattice constant. The tunneling strengths are given as products of transition dipole matrix elements that can be calculated as described in appendix B:

- $t_+ = -\frac{1}{8\pi\epsilon_0 a^3}\langle +_i\ 0_j|d^+_i d^-_j|0_i\ +_j\rangle = \frac{1}{8\pi\epsilon_0 a^3}|\langle +|d^+|0\rangle|^2$,
- $t_- = -\frac{1}{8\pi\epsilon_0 a^3}\langle -_i\ 0_j|d^-_i d^+_j|0_i\ -_j\rangle = \frac{1}{8\pi\epsilon_0 a^3}|\langle -|d^-|0\rangle|^2$,
- $w = -\frac{3}{8\pi\epsilon_0 a^3}\langle +_i\ 0_j|d^+_i d^+_j|0_i\ -_j\rangle = -\frac{3}{8\pi\epsilon_0 a^3}\langle -_i\ 0_j|d^-_i d^-_j|0_i\ +_j\rangle = \frac{3}{8\pi\epsilon_0 a^3}\langle -|d^-|0\rangle\langle +|d^+|0\rangle$.

The total Hamiltonian is given by

$$H = \frac{1}{2}\sum_{i\neq j}\hat{V}^{\text{dd}}_{ij} + \sum_i \boldsymbol{\psi}^\dagger_i \begin{pmatrix} \mu & 0 \\ 0 & -\mu \end{pmatrix} \boldsymbol{\psi}_i, \tag{1.13}$$

where the last sum includes the energy difference between the two orbitals.

According to [7] we have to break time-reversal symmetry to make the model topologically non-trivial. This can be done by making the two orbitals $|+\rangle$ and $|-\rangle$ distinguishable by choosing $\mu \neq 0$ or $t_+ \neq t_-$.

1.4. Band structure calculation

Band structures are calculated by going to reciprocal space. The reciprocal primitive vectors $\boldsymbol{b}_i$ are calculated from the real space lattice vectors $\boldsymbol{a}_i$. They span the reciprocal lattice whose primitive cell is the first Brillouin zone. Assuming two dimensions, we get the reciprocal primitive vectors [21] as

$$\boldsymbol{b}_1 = \frac{2\pi}{\boldsymbol{a}_{1,x}\boldsymbol{a}_{2,y} - \boldsymbol{a}_{1,y}\boldsymbol{a}_{2,x}} \begin{pmatrix} \boldsymbol{a}_{2,y} \\ -\boldsymbol{a}_{2,x} \end{pmatrix}, \tag{1.14}$$

$$\boldsymbol{b}_2 = \frac{2\pi}{\boldsymbol{a}_{1,x}\boldsymbol{a}_{2,y} - \boldsymbol{a}_{1,y}\boldsymbol{a}_{2,x}} \begin{pmatrix} -\boldsymbol{a}_{2,y} \\ \boldsymbol{a}_{2,x} \end{pmatrix}. \tag{1.15}$$

---

[2] This phase is a gauge dependent quantity. In order to get a well-defined, gauge invariant expression we have to look at the collected phase over closed loops.

The Hamiltonian can be brought into reciprocal space via a Fourier transform. We would like to get a general result that can be applied to several problems. For this purpose we assume that our real space Hamiltonian is of the form

$$H = \sum_j \boldsymbol{\psi}_j^\dagger \; G \; \boldsymbol{\psi}_j + \sum_{i\neq j} \boldsymbol{\psi}_i^\dagger \; F(\boldsymbol{R}_j - \boldsymbol{R}_i) \; \boldsymbol{\psi}_j, \tag{1.16}$$

where $\boldsymbol{\psi}_j$ is a vector of operators (e.g. a spinor), F a matrix-valued function of the distance vector $\boldsymbol{R}_j - \boldsymbol{R}_i$, and G a constant matrix. We can transform this Hamiltonian by substituting the operators with their Fourier representations using

$$\boldsymbol{\psi}_j = \frac{1}{\sqrt{N}} \sum_{\boldsymbol{k}} \boldsymbol{\psi}_{\boldsymbol{k}} \; \mathrm{e}^{\mathrm{i}\boldsymbol{k}\boldsymbol{R}_j}. \tag{1.17}$$

In order to get a simplified result we will use the following formulas:

$$\sum_j F(\boldsymbol{R}_j - \boldsymbol{R}_i)\mathrm{e}^{\mathrm{i}\boldsymbol{k}\boldsymbol{R}_j} = \mathrm{e}^{\mathrm{i}\boldsymbol{k}\boldsymbol{R}_i} \sum_j F(\boldsymbol{R}_j)\mathrm{e}^{\mathrm{i}\boldsymbol{k}\boldsymbol{R}_j} \qquad \text{shift theorem for DFT,} \tag{1.18}$$

$$\delta_{\boldsymbol{k},\boldsymbol{k}'} = \frac{1}{N}\sum_i \mathrm{e}^{\mathrm{i}(\boldsymbol{k}-\boldsymbol{k}')\boldsymbol{R}_i} \qquad \text{delta function in k-space.} \tag{1.19}$$

We obtain:

$$\begin{aligned} H &= \sum_j \boldsymbol{\psi}_j^\dagger \; G \; \boldsymbol{\psi}_j + \sum_{i\neq j} \boldsymbol{\psi}_i^\dagger \; F(\boldsymbol{R}_j - \boldsymbol{R}_i) \; \boldsymbol{\psi}_j \\ &= \sum_j \boldsymbol{\psi}_j^\dagger \; G \; \boldsymbol{\psi}_j + \sum_{i,j} \boldsymbol{\psi}_i^\dagger \; F(\boldsymbol{R}_j - \boldsymbol{R}_i) \; \chi_{\{\boldsymbol{R}_j - \boldsymbol{R}_i \neq 0\}} \; \boldsymbol{\psi}_j \\ &= \sum_{\boldsymbol{k},\boldsymbol{k}'} \delta_{\boldsymbol{k},\boldsymbol{k}'} \boldsymbol{\psi}_{\boldsymbol{k}'}^\dagger \; G \; \boldsymbol{\psi}_{\boldsymbol{k}} + \sum_{\boldsymbol{k},\boldsymbol{k}'} \delta_{\boldsymbol{k},\boldsymbol{k}'} \boldsymbol{\psi}_{\boldsymbol{k}'}^\dagger \; \sum_j F(\boldsymbol{R}_j) \; \chi_{\{\boldsymbol{R}_j \neq 0\}} \; \mathrm{e}^{\mathrm{i}\boldsymbol{k}\boldsymbol{R}_j} \; \boldsymbol{\psi}_{\boldsymbol{k}} \\ &= \sum_{\boldsymbol{k}} \boldsymbol{\psi}_{\boldsymbol{k}}^\dagger \left(G + \sum_{j\neq 0} F(\boldsymbol{R}_j) \; \mathrm{e}^{\mathrm{i}\boldsymbol{k}\boldsymbol{R}_j} \right) \boldsymbol{\psi}_{\boldsymbol{k}} \\ &\equiv \sum_{\boldsymbol{k}} \boldsymbol{\psi}_{\boldsymbol{k}}^\dagger \; E(\boldsymbol{k}) \; \boldsymbol{\psi}_{\boldsymbol{k}}. \end{aligned} \tag{1.20}$$

The eigenvalues of $E(\boldsymbol{k})$ build the band structure. Commonly it is plotted over the first Brillouin zone.

Application to the dipolar model on a square lattice

As an example we would like to apply this formula to the dipolar model on a square lattice. Here, we have $\boldsymbol{\psi}_i^\dagger = (b_{i,+}^\dagger, b_{i,-}^\dagger)$ and get

$$F(\boldsymbol{R}_j - \boldsymbol{R}_i) = \frac{a^3}{|\boldsymbol{R}_j - \boldsymbol{R}_i|^3} \begin{pmatrix} -t_+ & w\mathrm{e}^{-2\mathrm{i}\phi_{\boldsymbol{R}_j - \boldsymbol{R}_i}} \\ w\mathrm{e}^{2\mathrm{i}\phi_{\boldsymbol{R}_j - \boldsymbol{R}_i}} & -t_- \end{pmatrix}, \tag{1.21}$$

$$G = \begin{pmatrix} \mu & 0 \\ 0 & -\mu \end{pmatrix}. \tag{1.22}$$

Using these definitions we obtain the dipolar dispersion as it was calculated in [6]:

$$E(\boldsymbol{k}) = \begin{pmatrix} \mu & 0 \\ 0 & -\mu \end{pmatrix} + \sum_{j\neq 0} \frac{a^3}{|\boldsymbol{R}_j|^3} \begin{pmatrix} -t_+ & w\mathrm{e}^{-2\mathrm{i}\phi_{\boldsymbol{R}_j}} \\ w\mathrm{e}^{2\mathrm{i}\phi_{\boldsymbol{R}_j}} & -t_- \end{pmatrix} \mathrm{e}^{\mathrm{i}\boldsymbol{k}\boldsymbol{R}_j} = n^0_{\boldsymbol{k}}\, \mathbb{1} + \boldsymbol{n}_{\boldsymbol{k}} \cdot \boldsymbol{\sigma}. \tag{1.23}$$

The equation includes the spin-independent hopping $n^0_{\boldsymbol{k}} = -\frac{t^- + t^+}{2}\epsilon^0_{\boldsymbol{k}}$ and a vector containing all information about the spin-orbit coupling

$$\boldsymbol{n}_{\boldsymbol{k}} = \begin{pmatrix} w \ \mathrm{Re}\ \epsilon^2_{\boldsymbol{k}} \\ w \ \mathrm{Im}\ \epsilon^2_{\boldsymbol{k}} \\ \mu + \frac{t^- - t^+}{2}\epsilon^0_{\boldsymbol{k}} \end{pmatrix} \tag{1.24}$$

with

$$\epsilon^m_{\boldsymbol{k}} = \sum_{j\neq 0} \frac{a^3}{|\boldsymbol{R}_j|^3} \mathrm{e}^{\mathrm{i}\boldsymbol{k}\boldsymbol{R}_j + im\phi_{\boldsymbol{R}_j}}. \tag{1.25}$$

From this vector, we can calculate the dispersion relation $E_\pm(\boldsymbol{k}) = n^0_{\boldsymbol{k}} \pm |\boldsymbol{n}_{\boldsymbol{k}}|$ as well as the Chern number thanks to equation 1.9.

Application to the dipolar model on a lattice with a two-atom basis

If we have a lattice with a two-atom basis[3], $\boldsymbol{\psi}^\dagger_i$ will be a vector of four operators: $\boldsymbol{\psi}^\dagger = (b^\dagger_{A,j,+}, b^\dagger_{A,j,-}, b^\dagger_{B,j,+}, b^\dagger_{B,j,-})$. Here, $b^\dagger_{A,j,\pm}$ acts on the sublattice A and $b^\dagger_{B,j,\pm}$ acts on the sublattice B. In this case F and G are 4×4 matrices that can be written as

$$F(\boldsymbol{R}_j - \boldsymbol{R}_i) = \begin{pmatrix} F^{AA} & F^{AB} \\ F^{BA} & F^{BB} \end{pmatrix}, \tag{1.26}$$

$$G = \begin{pmatrix} G^A & 0 \\ 0 & G^B \end{pmatrix} \tag{1.27}$$

with

$$F^{XY} = \frac{a^3}{|\boldsymbol{R}_{Y,j} - \boldsymbol{R}_{X,i}|^3} \begin{pmatrix} -t_+ & w\mathrm{e}^{-2\mathrm{i}\phi_{\boldsymbol{R}_{Y,j}-\boldsymbol{R}_{X,i}}} \\ w\mathrm{e}^{2\mathrm{i}\phi_{\boldsymbol{R}_{Y,j}-\boldsymbol{R}_{X,i}}} & -t_- \end{pmatrix}, \tag{1.28}$$

$$G^X = \begin{pmatrix} \mu & 0 \\ 0 & -\mu \end{pmatrix}. \tag{1.29}$$

We see from $\boldsymbol{R}_{A,i} = \boldsymbol{R}_{A,0} + \boldsymbol{R}_i$ and $\boldsymbol{R}_{B,j} = \boldsymbol{R}_{B,0} + \boldsymbol{R}_j$, that F is indeed a function of $\boldsymbol{R}_j - \boldsymbol{R}_i$.

---

[3] We can handle lattices with a larger basis in a similar way.

2. Calculating a band structure analogue for finite systems

As pointed out in the chapter before, a signature of topological bands is the existence of edge states in systems with boundaries.

One nicely sees the edge states in the band structures of half-finite systems[1]. However, such systems cannot be realized experimentally. For experiments, systems have to be finite. Actually, systems where one has control over individual atoms can only be realized with few particles. It already requires strong efforts to obtain arrays with few tens of atoms [22]. In addition, some numerical methods such as exact diagonalization rely on systems with similarly small atom numbers [23].

Since it is questionable whether it is valid to transfer results obtained for infinite systems to such small arrays of atoms, we have to analyze them separately. Since the normal band structure cannot be calculated for them, one has to examine them differently. The standard procedure is to look at their density of states. Unfortunately, it provides only little information. Indeed, it usually tells when edge states cross band gaps. But further information that are present in the band structure are lost in the density of states, see figure 2.1.

For example, the density of states can not tell you how many edge states exist and how their dispersion relations are. Hence the density of states is not sufficient for investigating edge states in detail. Likewise, the density of states does not help if one tries to get the Chern numbers via the bulk-edge correspondence.

In this chapter we develop a new tool that will allow us to solve these problems: We construct a band structure analogue for completely finite systems. It will work for arbitrary two-dimensional systems. But for ease of reading, we first do not consider the general case: Let us imagine that we have a C_n symmetric, disk-shaped system as shown in figure 2.2. Furthermore we assume that we deal with a model that has only one single kind of excitations. The Haldane model fulfills this requirement. Thus we will use it for example plots[2].

Later we will generalize our approach to systems with no symmetries. Additionally we will show how it can be adapted to our dipolar model that has two different kinds of excitations, namely excitations to the $|+\rangle$ and $|-\rangle$ orbitals.

---

[1] Half-finite systems are systems that are finite in one direction and infinite in the other.

[2] The parameters for the plots will be $t_1 = 2$, $t_2 = 1$, $\mu = 0$, and $\phi = \pi/2$.

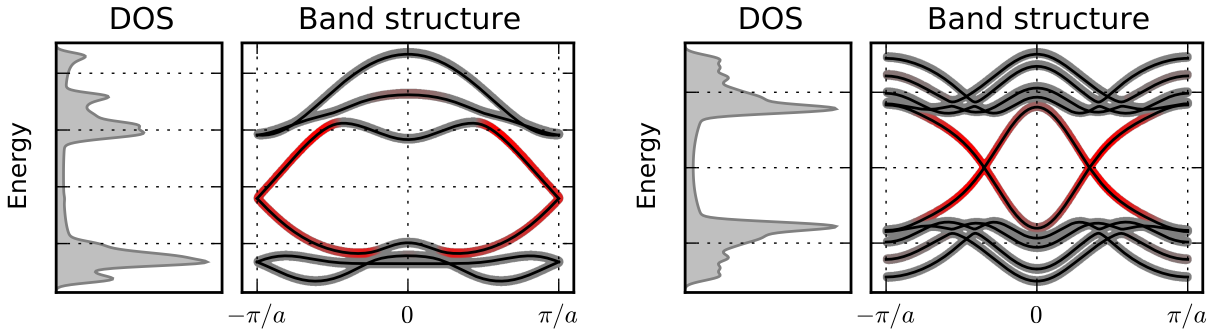

(a) Two edge states.

(b) Four edge states.

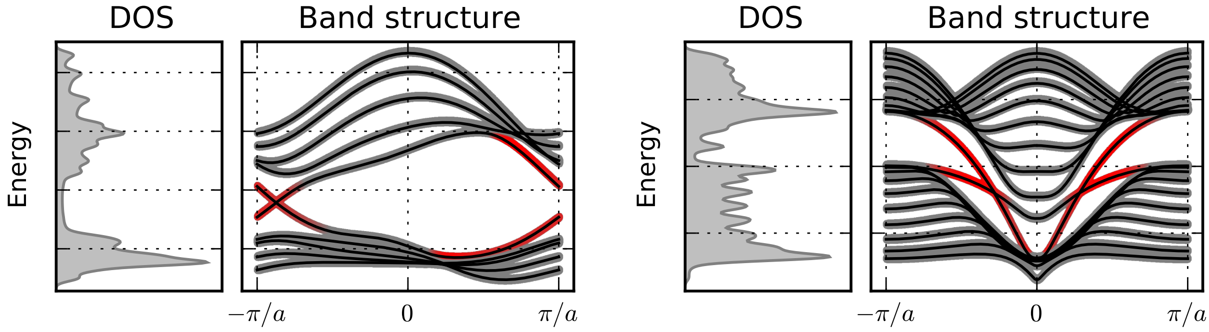

(c) Edge states with different dispersions.

(d) Energetically “hidden” edge states.

Fig. 2.1.: Band structures of four different, generic half-finite systems with edge states (i.e. states, that mainly live at the edge of the half-finite systems), that are colored in red. The corresponding density of states (DOS) is plotted to illustrate how much information about edge states is lost in the density of states. For example, it can not show the quantity and dispersion of edge states. Sometimes we can not even recognize the existence of edge states in the density of states.

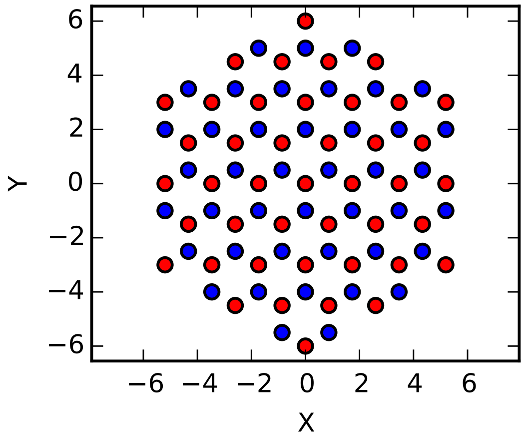

Fig. 2.2.: Cutout from an honeycomb lattice as example of a C_n symmetric system where the order of rotational symmetry n is 3. The two sublattices of the honeycomb lattice are painted in different colors.

2.1. Bloch's theorem for C_n symmetric systems

The generator of the rotation group C_n is the rotation by $2\pi/n$. We call its representation on the Hilbert space $D_{2\pi/n}$. "C_n symmetric" or "rotational symmetric of order n" means, that $D_{2\pi/n}$ commutes with the Hamiltonian:

$$[H, D_{2\pi/n}] = 0. \tag{2.1}$$

Bloch's theorem states in its original form, that for particles in a translational periodic crystal there is a basis of energy eigenfunctions

$$|\Psi^k(r)\rangle = \exp(ikr)\ |u^k(r)\rangle, \text{ where } u^k \text{ has the same periodicity as the crystal.} \tag{2.2}$$

The proof of Bloch's theorem [21] relies on the fact, that the translation operators which shift the crystal by multiples of the lattice constant commute with the Hamiltonian and commute among each others.

In our case, both are properties of the rotation operators which can be expressed as powers of $D_{2\pi/n}$. Hence we can formulate Bloch's theorem for rotations instead of translations

$$|\Psi^{m,l}(\alpha)\rangle = \exp(im\alpha)\ |u^{m,l}(\alpha)\rangle, \text{ where } u^{m,l}(\alpha) = u^{m,l}(\alpha + 2\pi/n\ p),\ p \in \mathbb{Z}. \tag{2.3}$$

The index l takes into account that there can be more than one state for one angular quasimomentum $m \in \{0, ...n-1\}$.

Equation 2.3 can be written in matrix representation using e.g. the basis set $\{|b_1\rangle, ...|b_N\rangle\}$ where $|b_j\rangle$ has an excitation at site j.

$$\begin{pmatrix} \boldsymbol{\Psi}_1 \\ \vdots \\ \boldsymbol{\Psi}_N \end{pmatrix} = \begin{pmatrix} \exp(im\alpha_1) & & \\ & \ddots & \\ & & \exp(im\alpha_N) \end{pmatrix} \begin{pmatrix} \boldsymbol{u}_1 \\ \vdots \\ \boldsymbol{u}_N \end{pmatrix}. \tag{2.4}$$

In the following we use the abbreviating notation

$$\boldsymbol{\Psi} = \exp(im\alpha)\ \boldsymbol{u}. \tag{2.5}$$

In this equation, $\boldsymbol{\Psi} = (\langle b_1|\Psi^{m,l}(\alpha)\rangle, ...\langle b_N|\Psi^{m,l}(\alpha)\rangle)^T$ is an eigenvector of the Hamiltonian matrix and α a diagonal matrix with $\alpha_1, ...\alpha_N$ on its diagonal. The vector $\boldsymbol{u} = (\langle b_1|u^{m,l}(\alpha)\rangle, ...\langle b_N|u^{m,l}(\alpha)\rangle)^T$ is invariant under C_n rotations. As a result of this, its elements repeat n times[3].

2.2. Discrete band structure

By diagonalizing the Hamiltonian matrix we get the eigenstates $\boldsymbol{\Psi}$ of our system. Their angular quasimomentum m can be determined by making use of equation 2.5. In order

---

[3] Actually, this is only true, if we have no lattice site in the center of rotation. If there is one, we simply neglect it and everything is correct again.

to do so, we guess a quasimomentum M, calculate $\boldsymbol{w} \equiv \exp(-\mathrm{i}M\alpha)\ \boldsymbol{\Psi}$, and analyze the result[4]. For doing the analysis, we have several possibilities. The obvious approach would be to count how often the elements of $\boldsymbol{w}$ are repeated, as it is shown in figure 2.3. If they repeat n times, we have $\boldsymbol{w} = \boldsymbol{u}$ and our guess was correct[5]. Otherwise we have to try a different M.

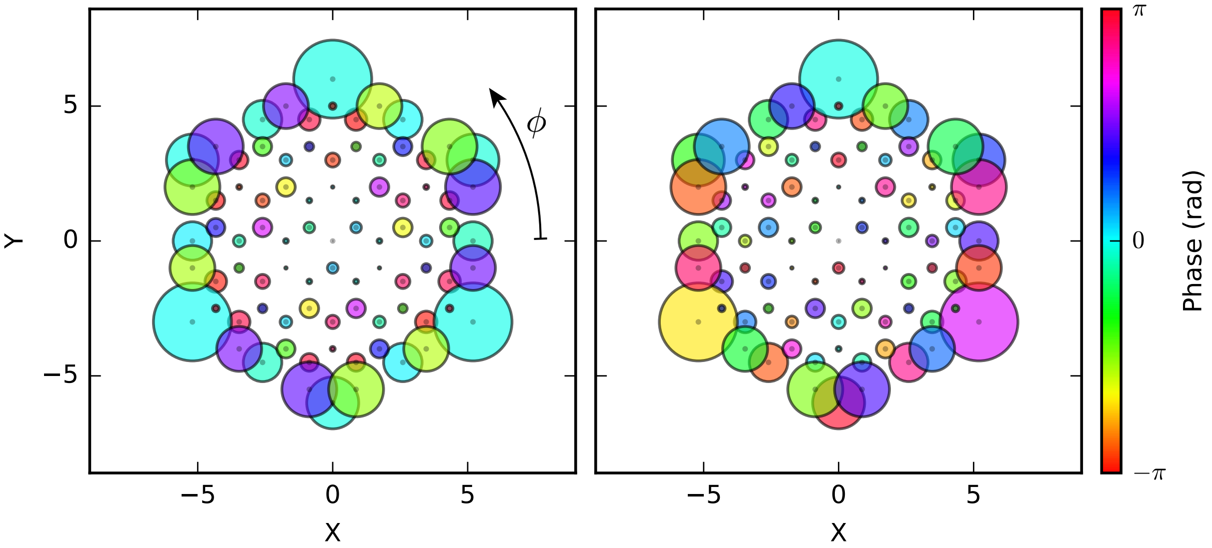

Fig. 2.3.: Visualizations of the vector $\boldsymbol{w} = \exp(-\mathrm{i}M\alpha)\boldsymbol{\Psi}$. Here, $\boldsymbol{\Psi}$ is an edge state eigenvector of the Haldane Hamiltonian. M is the guessed angular quasimomentum. The area of the bubbles is proportional to the probability to find the state on a lattice site. The color indicates the phase of the wave function. The visualization is shown for a correct guess (left) as well as for a wrong one (right). In the first case, the visualization has a threefold symmetry: As we go along ϕ the patterns repeat three times. This is due to the fact that for the correct guess $\boldsymbol{w} = \boldsymbol{u}$ is invariant under C_n rotations. For the wrong guess, there is no such symmetry in the pattern of colors.

In the following we describe another procedure for the determination of m that relies on autocorrelations. A benefit of the new method is that one does not need to know the value n of the order of the symmetry in advance.

As before, we guess a quasimomentum M and calculate $\boldsymbol{w} = \exp(-\mathrm{i}M\alpha)\boldsymbol{\Psi}$. Now we compute the autocorrelation of $\boldsymbol{w}$ as function of ϕ (see figure 2.3). In order to do so, we label the basis elements with the radial and angular position of the site, i.e. $|b_j\rangle$ becomes $|b_{r,\alpha}\rangle$. This implies that we can label the coordinates of the $\boldsymbol{w}$ vector with r and α, too.

---

[4] For this to work it is necessary that eigenstates with different quasimomenta are non-degenerate. In case of degeneracy it becomes more complicated. Fortunatelly, this rarely happens in our systems.

[5] To be precise, we can only figure out whether a guess modulo n was correct. We can circumvent this problem if we do the test with the series of natural numbers starting from zero. Then, the smallest number that pass the test is the appropriate guess.

It allows us to compute the autocorrelation of $\boldsymbol{w}$ in the following way

$$\begin{aligned} AC(\phi) &= \sum_{r,\alpha} \boldsymbol{w}_{r,\alpha}{}^* \cdot \boldsymbol{w}_{r,\alpha+\phi} = \sum_{r,\alpha} \exp(\mathrm{i}M\alpha)\ \boldsymbol{\Psi}_{r,\alpha}{}^* \cdot \exp(-\mathrm{i}M(\alpha+\phi))\ \boldsymbol{\Psi}_{r,\alpha+\phi} \\ &= \sum_{r,\alpha} \exp(\mathrm{i}(M-m)\alpha)\ \boldsymbol{u}_{r,\alpha}{}^* \cdot \exp(\mathrm{i}(m-M)(\alpha+\phi))\ \boldsymbol{u}_{r,\alpha+\phi} \\ &= \exp(\mathrm{i}(m-M)\phi) \sum_{r,\alpha} \boldsymbol{u}_{r,\alpha}{}^* \cdot \boldsymbol{u}_{r,\alpha+\phi}. \end{aligned} \tag{2.6}$$

This result is powerful. As we shall see, it can tell us the order n of the rotational symmetry as well as the angular quasimomentum m. A minor flaw is that this autocorrelation can be non-zero only if lattice sites rotated by ϕ precisely encounter unrotated sites. Hence, a plot of the autocorrelation would be zero for almost all values of ϕ. To tackle this visualization problem we use discretized polar coordinates, so that lattice sites can exclusively be at discrete positions in space. In this coordinate system, ϕ can take discrete values only. Then, rotated sites will encounter unrotated sites for all values of ϕ, provided that we use a sufficently rough discretization. This solves our visualization problem. We use this technique for figures 2.4 and 2.5.

2.2.1. Order of rotational symmetry

To determine the order n we calculate the absolute value of the autocorrelation 2.6.

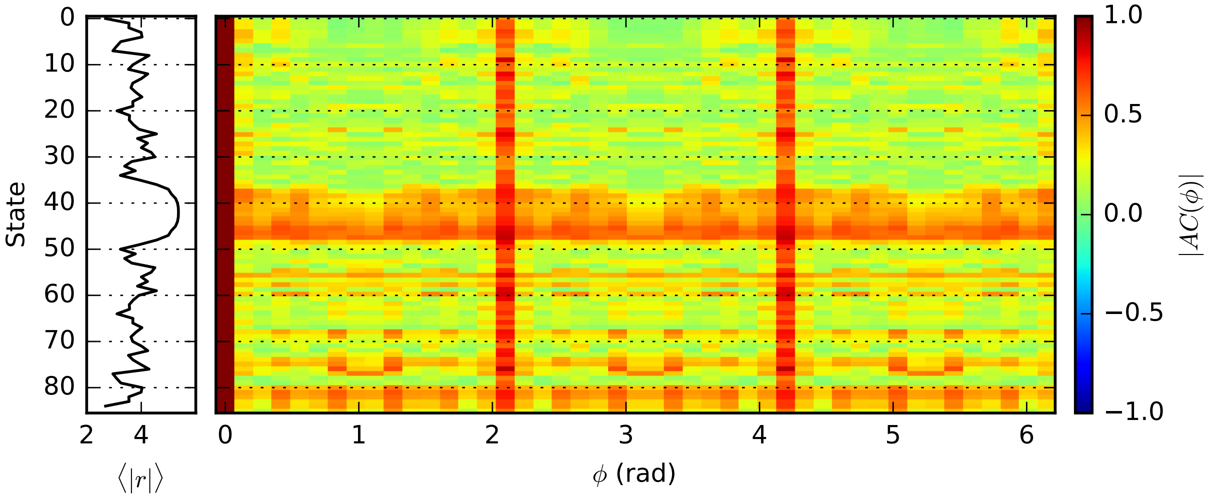

Fig. 2.4.: We consider the Haldane model on the C_3 symmetric disk shown in figure 2.2. For all eigenstates $\boldsymbol{\Psi}$ of the Hamiltonian the absolute value of the autocorrelation of $\boldsymbol{w} = \exp(-\mathrm{i}M\alpha)\boldsymbol{\Psi}$ is plotted as a function of the rotation ϕ (the same color map as for figure 2.5 is used to enhance comparability). Here, the value of M does not matter. The eigenstates $\boldsymbol{\Psi}$ are labeled according to their energy, i.e. the higher the index label the larger the energy is. The three red columns occur because of the C_3 symmetry. On the left hand side we display the location of the eigenstates. Hereto the expectation value of the radial coordinate is plotted. A large expectation value means that the corresponding state is an edge state.

It is given by

$$|AC(\phi)| = \left| \sum_r \sum_\alpha \boldsymbol{u}_{r,\alpha}{}^* \cdot \boldsymbol{u}_{r,\alpha+\phi} \right| = |\boldsymbol{u}_{\text{unrotated}}{}^* \cdot \boldsymbol{u}_{\text{rotated by }\phi}|. \tag{2.7}$$

Note, that it is independent of the guessed M. Hence, we can use $M = 0$ and calculate the absolute autocorrelation directly from the eigenstates. It is shown in figure 2.4.

If $\boldsymbol{u}_{\text{rotated by }\phi}$ equal $\boldsymbol{u}_{\text{unrotated}}$ up to a global phase, the autocorrelation is one. This is the case for $\phi = 2\pi/n\ p$ since $\boldsymbol{u}$ is invariant under C_n rotations. If both vectors are different, the absolute value of the autocorrelation is smaller than one. Due to this observation we can determine n by looking at the angles where $|AC(\phi)|$ is one. The first non-zero angle where this is the case is $\phi_1 \equiv 2\pi/n$. This immediately gives us n.

2.2.2. Angular quasimomentum

In order to get the angular quasimomentum m, we consider the real part of the autocorrelation 2.6 for $\phi = \phi_1$

$$\text{Re } AC(\phi_1) = \cos(2\pi(m - M)/n). \tag{2.8}$$

In figure 2.5, it is shown for all angles.

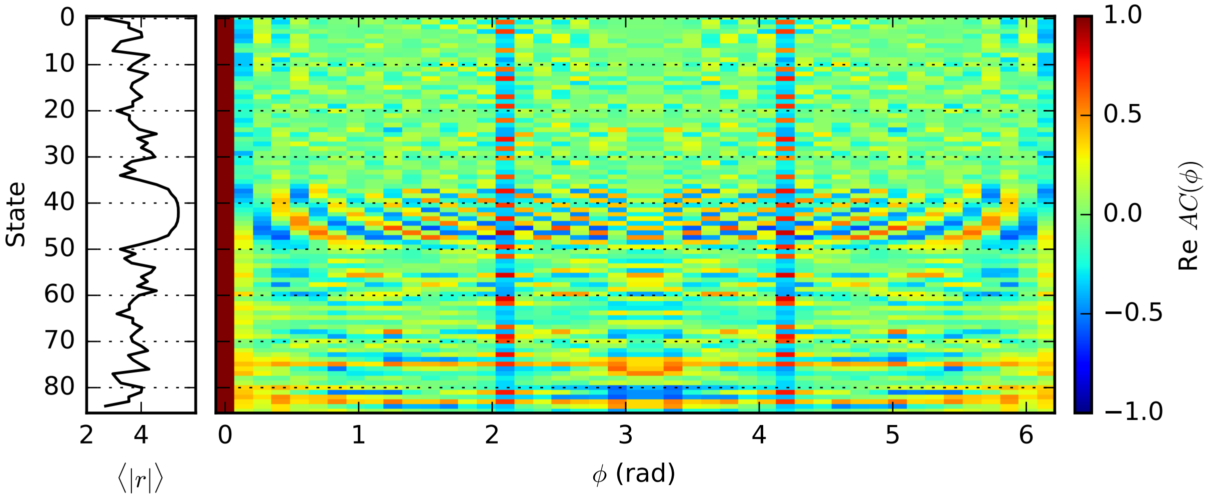

Fig. 2.5.: Plots similar to the ones shown in figure 2.4. The only difference is that now the real part — and not the absolute value — of the autocorrelation of $\boldsymbol{w} = \exp(-\mathrm{i}M\alpha)\boldsymbol{\Psi}$ is drawn. Here, M is choosen to be 1.

Let us recall, $m \in \{0, ...n - 1\}$ is the angular quasimomentum that the eigenstate actually has. M is our guess for the quasimomentum. Like m, it should be between 0 and $n - 1$. Then Re $AC(\phi_1)$ is one, if and only if our guess was correct. This allows us to numerically determine the angular quasimomentum of the eigenstates.

2.2.3. Construction of the discrete band structure

If we compare Bloch's original theorem for translations with the one written down for rotations, we see that the angular quasimomentum m plays the role of the quasimomentum k. We are primarily interested in describing edge states, i.e. states that mainly live on the boundary of a finite system. Here, the analogy between m and k gets apparent: On the one hand the edge of a disk-shaped system can be seen as a circle. On the other hand it can be interpreted as one dimensional system with periodic boundary conditions. In the first picture one would name the quasimomentum m, in the second one k.

The obvious way to analyze a periodic one dimensional system is to calculate its discrete band structure over k. Because of the analogy pointed out above, we would like to look at the discrete band structure over m for finite C_n symmetric systems. For this we plot the energies of the eigenstates over their angular quasimomentum m. The space of all possible m can be understood as reduced Brillouin zone. The result can be seen in figure 2.6. From it we can already get an impression of the edge states dispersion relation. However, the plot is a bit messy. In the next section we come up with an improved band structure analogue.

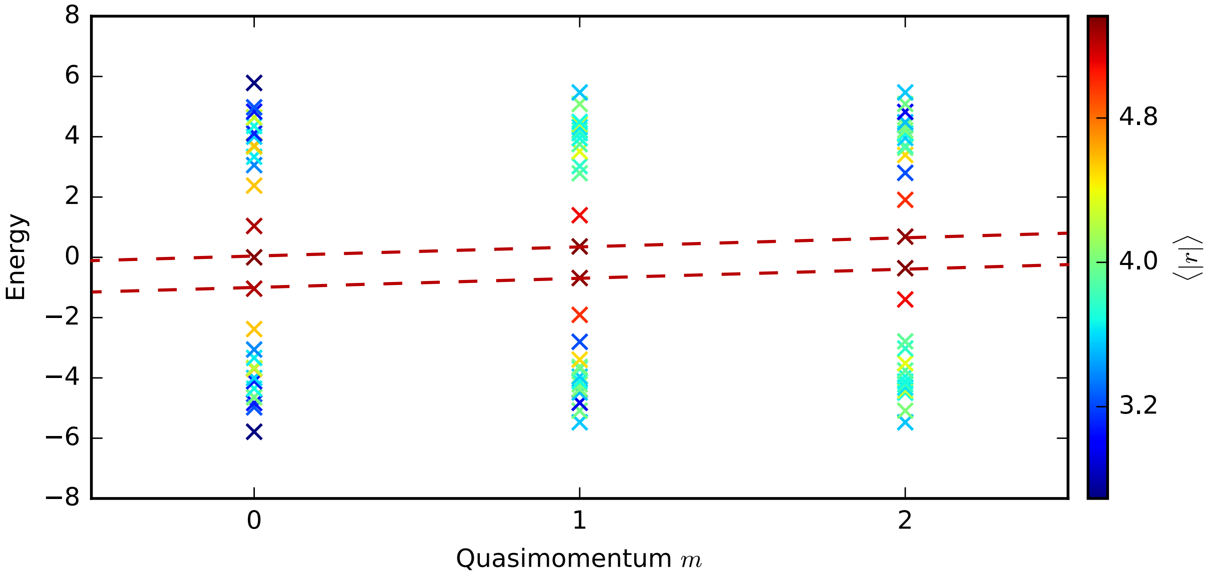

Fig. 2.6.: Discrete band structure calculated for the Haldane Hamiltonian. The computation was performed for the lattice geometry shown in 2.2. The color of the points encodes the expectation value of the radial coordinate calculated for the corresponding eigenvector. Red colored points belong to edge states. They show a pattern that suggests that there is a linear dispersion relation. The dashed lines serve as a guide to the eye.

2.3. Unwrapped band structure

Figure 2.4 shows that the absolute value of the autocorrelation function for edge states has high values for angles $\phi \neq 2\pi/n\ p$, too. This suggests that edge states possess higher symmetry than other states. Why this is the case becomes clear, if we look at the edge of a C_n symmetric system: Its rotational symmetry is almost of the order $q \cdot n$, where q is a integer number that is the larger the bigger the system is. This is illustrated in figure 2.7.

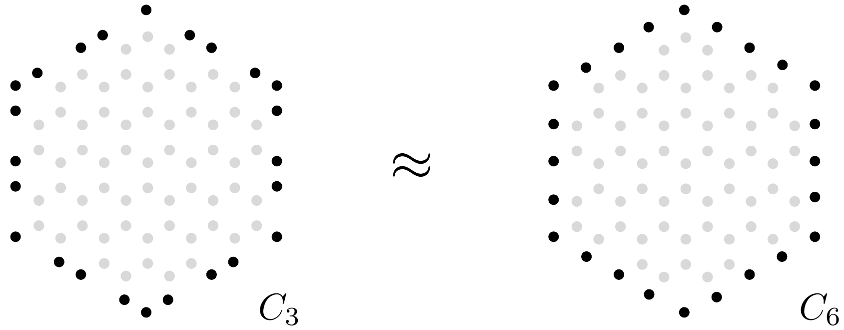

Fig. 2.7.: In approximation, the edge of a C_3 symmetric system (e.g. the edge of the system shown in figure 2.2) has a rotational symmetry of an order higher than 3. The approximation works the better the larger the system is.

Rotational symmetry of a q times higher order would imply a q times larger Brillouin zone. This suggests to use different reduced Brillouin zones for bulk and edge states. But since this would get complicated, we decide to plot the band structure over the extended Brillouin zone. In the following we describe how to get it.

Since the band structure over the reduced Brillouin zone can be easily calculated from the band structure over the extended one[6], it seems natural to try it the other way round — especially as we already calculated the band structure over the reduced Brillouin zone in the last section. However, it becomes apparent that this is very difficult. It is not clear how to "unwrap" the band structure over the reduced Brillouin zone: There are countless ways how the bands could be stitched together to obtain the band structure over the extended Brillouin zone. Hence we choose a different approach.

Let us start with a general look at a band structures over the extended Brillouin zone. Apparently, the band structure can be seen as a specific allocation of eigenenergies and eigenvectors $\mathbf{\Psi}$ to the quasimomenta m_{ext} of the extended zone (in the following we write $\mathbf{\Psi}(m_{\text{ext}})$ for the eigenvector that is allocated to the quasimomentum m_{ext}). Our goal now is to find this specific allocation. For this purpose we investigate properties of band structures over extended Brillouin zones.

---

[6] The quasimomenta m_{red} of the reduced Brillouin zone can be obtained from the quasimomenta m_{ext} of the extended one through $m_{\text{red}} = m_{\text{ext}} \bmod 2\pi/a$. This implies that the band structure gets "wrapped" if we switch from the extended to the reduced Brillouin zone.

For all quasimomenta m_{ext}, where no avoided crossing are, the following holds: The periodic part of the Bloch function (in our case the vector $\boldsymbol{u}$) does not change fast with m_{ext}[7]. This implies that the overlaps between vectors $\boldsymbol{u}$ that belong to neighboring points in the band structure, i.e. $o(m_{\text{ext}}) = |\boldsymbol{u}(m_{\text{ext}}+1)^* \cdot \boldsymbol{u}(m_{\text{ext}})|^2$, should be large. This suggests the following:

> The allocation of the eigenvectors $\boldsymbol{\Psi}$ to the quasimomenta m_{ext} should be made in such a way that the sum of all overlaps $\sum_{m_{\text{ext}}} o(m_{\text{ext}})$ is as large as possible.

As we shall see later, this demand actually gives us convenient results.

Using equation 2.5, we can calculate the overlap directly from the eigenvectors:

$$\begin{aligned} o(m_{\text{ext}}) &= |\boldsymbol{u}(m_{\text{ext}+1})^* \cdot \boldsymbol{u}(m_{\text{ext}})|^2 && (2.9)\\ &= |(\exp(-\mathrm{i}(m_{\text{ext}}+1)\alpha)\boldsymbol{\Psi}(m_{\text{ext}}+1))^* \cdot \exp(-\mathrm{i}m_{\text{ext}}\alpha)\boldsymbol{\Psi}(m_{\text{ext}})|^2 && (2.10)\\ &= |\boldsymbol{\Psi}(m_{\text{ext}}+1)^* \cdot \exp(\mathrm{i}\alpha)\boldsymbol{\Psi}(m_{\text{ext}})|^2, && (2.11) \end{aligned}$$

where $\exp(\mathrm{i}\alpha)$ adds one to the momentum of the eigenvector $v(m_{\text{ext}})$. Hence, o is the overlap of two eigenvectors after increasing the momentum of one of them by one. Which eigenvectors are represented by $v(m_{\text{ext}}+1)$ and $v(m_{\text{ext}})$ depends on the selected allocation. In figure 2.8, the overlaps are shown for all possible combinations of eigenvectors.

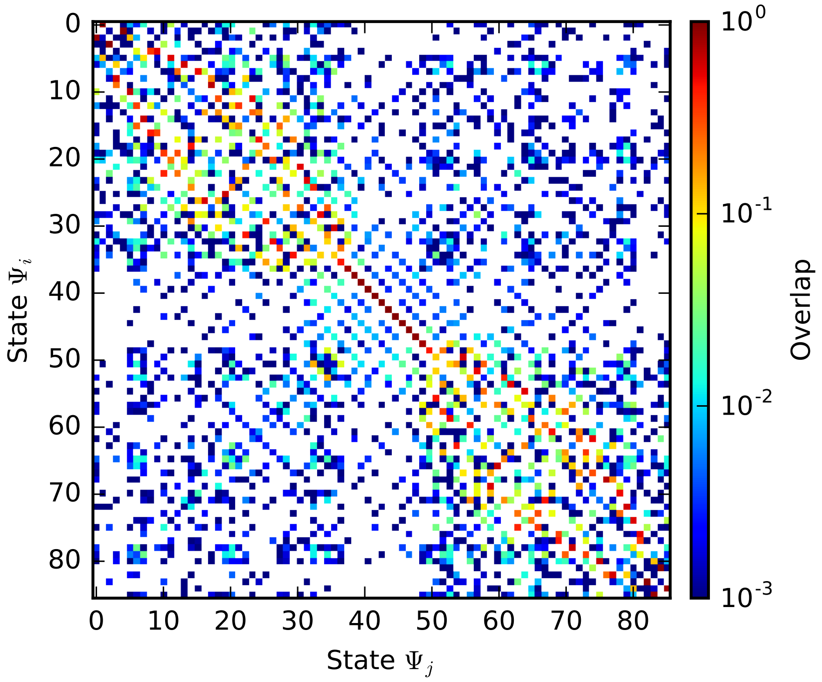

Fig. 2.8.: Overlap $|\boldsymbol{\Psi}_i^* \cdot \exp(\mathrm{i}\alpha)\boldsymbol{\Psi}_j|$ for all possible combinations of eigenvectors. As for the previous plots, the eigenvectors $\boldsymbol{\Psi}$ are computed for the Haldane model on the lattice shown in 2.2. The overlap is plotted in logarithmic colors. If the overlap has a value of approximatively zero, the color is white.

---

[7] This does not hold for the Bloch functions themselves. If they have the same periodic part, they are orthogonal to each other.

The zero pattern in figure 2.8 comes in large parts from the C_3 symmetry of the system for that the eigenvectors have been computed. In case of C_3 symmetry we can calculate a reduced angular momentum $m_{\text{red}} \in \{0, 1, 2\}$ for all eigenvectors — like we did it in the last section. One can show that the overlap $o = |\mathbf{\Psi}_i^* \cdot \exp(\mathrm{i}\alpha)\mathbf{\Psi}_j|$ can be non-zero only if

$$(m_{\text{i, red}} - m_{\text{j, red}}) \bmod 3 = 1. \tag{2.12}$$

This requirement is fulfilled only if bands from the reduced Brillouin zone are stitched together, i.e. if the band structure over the reduced Brillouin zone is unwrapped. Through this we automatically take into account that the band structure over the extended Brillouin zone should result out of the band structure over the reduced one. Our postulation that the total overlap should be maximized does not need to be modified.

Now we would like to determine the allocation that maximizes the total overlap. In order to do so we have to solve an optimization problem. In principle we could calculate the total overlap for all possible allocations and chose the one for which it is maximal. However, the number of possible allocations scales like $N!$ where N is the number of eigenstates, so that the suggested approach is not feasible. Our optimization problem is NP-hard since we can map it to the “traveling salesman problem” (TSP) where a salesman tries to visit cities on the shortest possible route [24]: In our case, the reciprocal overlap between eigenvectors corresponds to the distance between cities. Fortunately, the TSP is well-investigated so that a lot of heuristic solving strategies exist. Our mapping allows us to apply them to our problem. We will use a version of “ant colony optimization”[8] because it is intuitive to understand, easy to implement, and yet powerful [25].

Using this method we finally obtain the unwrapped band structure. An example is shown in figure 2.10.

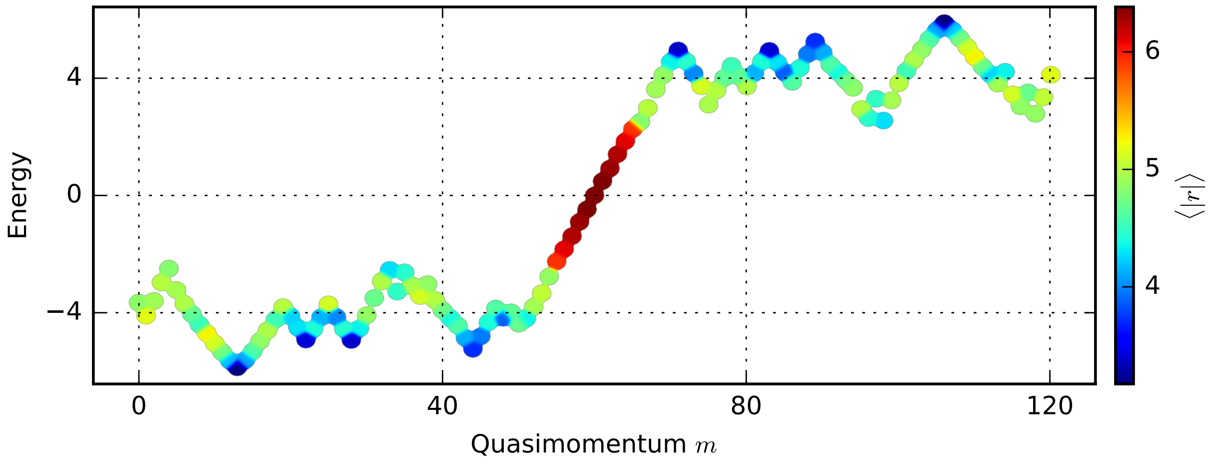

Fig. 2.9.: Unwrapped band structure calculated for the Haldane Hamiltonian. The edge state with its linear dispersion relation is nicely visible. The zigzag structures belong to the bulk bands.

---

[8] Since the ant colony optimization algorithm is a heuristic method, it is not guaranteed that the found solution is optimal. However, it turns out to be sufficiently good for our purposes.

2.4. Generalizations

We can generalize our approach to systems with no symmetries using the following idea:

Let us assume that our system has a well-defined boundary that we can interpret as a one dimensional, periodic system. Then, we can label every position on the boundary with a parameter q. If we determine for each lattice site the position on the edge that is closest to it, we can assign the parameter q to sites in the bulk as well. Using a second parameter s that specifies the distance from the edge, we can label all lattice sites with new coordinates. They can be used in the same way as the coordinates α, r that we have applied for rotational symmetric systems. For example, we can calculate the autocorrelation of $\boldsymbol{w}$ as a function of q instead of α. Using this trick, we can obtain the discrete and unwrapped band structure for Haldane systems with no rotational symmetries.

In order to calculate them for our dipolar model, we have to slightly modify our methods again. Now, the quasimomentum m is not a good quantum number:

Let us assume that we have a rotational symmetric state with one excitation to the $|+\rangle$ orbital and $m = 0$. If we apply our dipolar operator 1.3 on this state, it gets coupled to the state with one excitation to the $|-\rangle$ orbital and $m = 2$. However, in case of a C_n symmetric system, the quantity

$$\tilde{m} = (m + \sigma) \bmod n, \text{ with } \sigma = \pm 1 \text{ for } |\pm\rangle \tag{2.13}$$

is still conserved. Thus, we have to use this quantum number instead of m for our dipolar system. As an example, we calculate the unwrapped band structure for a disk-shaped cutout from a square lattice. We obtain two edge states, since the dipolar model on a square lattice give rise to bands with Chern numbers of ± 2 [6].

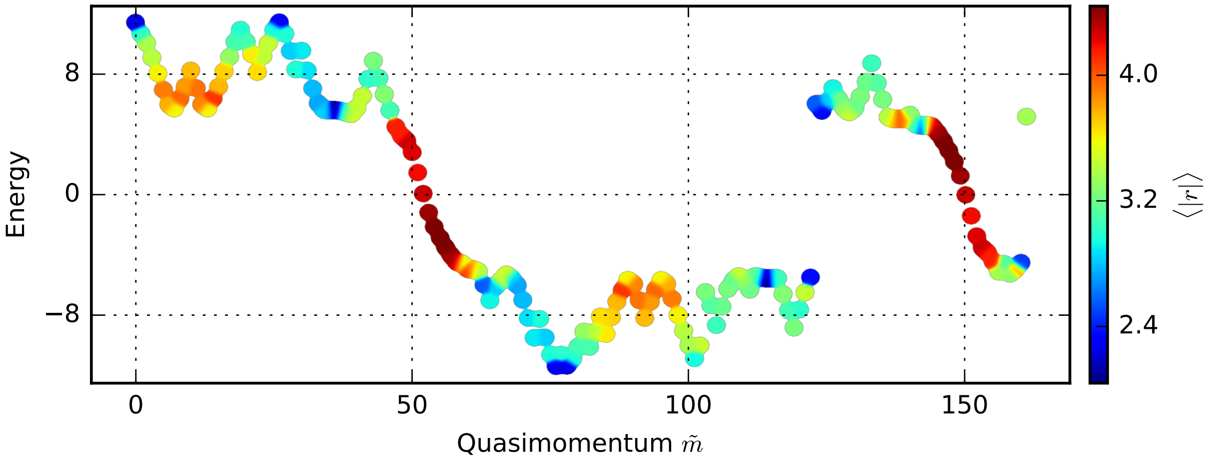

Fig. 2.10.: Unwrapped band structure for our dipolar system using a cutout from a square lattice.

Further unwrapped band structures are shown in the next chapter, see figure 3.9 and 3.11.

3. Experimental proposals for cold gases setups

In this chapter, we propose a realization of topological bands that is based on our dipolar model (see [6] and its description in the introduction 1.3). For the realization, we need particles with a strong dipolar interaction, for example polar molecules or Rydberg atoms. In this thesis, we focus on Rydberg atoms, since they have some properties that we would like to make use of later. The following proposal was designed in cooperation with Thierry Lahaye and Antoine Browaeys and is well suited for their Rydberg setup [22, 26].

For implementing the dipolar model, our atoms should possess a level structure as shown in figure 1.3 of the introduction. In this proposal, we use ^{87}Rb atoms and states from the $|63S_{1/2}\rangle$ and $|62P_{3/2}\rangle$ manifolds. We employ $S_{1/2}$ and $P_{3/2}$ states to have as few levels as possible inside the manifolds. The principle quantum numbers are chosen such that the interaction strength results in time scales that are well suited for experiments. Assuming that we have a deep optical lattice with one Rydberg atom per site, we apply static fields perpendicular to the lattice to manipulate the level structure of the atoms. As shown in 3.1 we can isolate the V level scheme, that is required for our model, via the Stark and Zeeman effect.

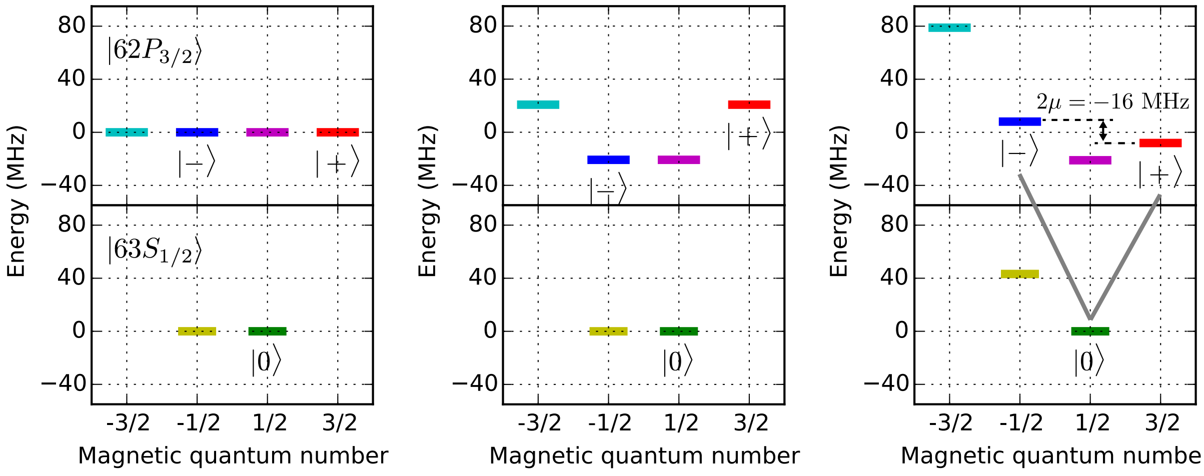

(a) Without fields. *(b)* $E = 600\,\mathrm{mV/cm}$ added. *(c)* $B = -15.6\,\mathrm{G}$ in addition.

Fig. 3.1.: Designing the level structure. The lower plots show the $|63S_{1/2}\rangle$ manifold, the upper ones the $|62P_{3/2}\rangle$ manifold. With the help of the Zeeman and Stark effect we isolate the V level scheme.

For an explanation of the Stark and Zeeman effect as well as for the calculations, see appendix C and D. The fields are chosen be sufficiently strong for isolating the V level scheme but weak enough to ensure a negligible level mixing: The overlap of the resulting states with the unperturbed ones is still 94 %-97 %. The fields can be used to tune the difference in energy $\mu = \left(E(|-\rangle) - E(|+\rangle)\right)/2$ of the two orbital states. This is the only controllable parameter of the model since the tunneling strengths are fixed by the dipole matrix elements as explained in section 1.3 (for their calculation see appendix B). Given a lattice constant of $a = 10\,\mu\mathrm{m}$, we have $t_+ = 2.41\,\mathrm{MHz}$, $t_- = 0.80\,\mathrm{MHz}$, and $w = 4.17\,\mathrm{MHz}$. We choose a large lattice constant because the pair potentials get complicated for small interatomic distances [27].

It is a nice property of our system, that t_+ and t_- are intrinsically different so that we need no microwave dressing. Actually, this is one advantage over the realization with polar molecules as it was described in [6]. The advantage results from the different Clebsch–Gordan coefficients for the $\langle +|d^+|0\rangle$ and $\langle -|d^-|0\rangle$ transitions in our system.

To find out whether the states of the V scheme are really energetically separated we have to look at the pair states energies in figure 3.2.

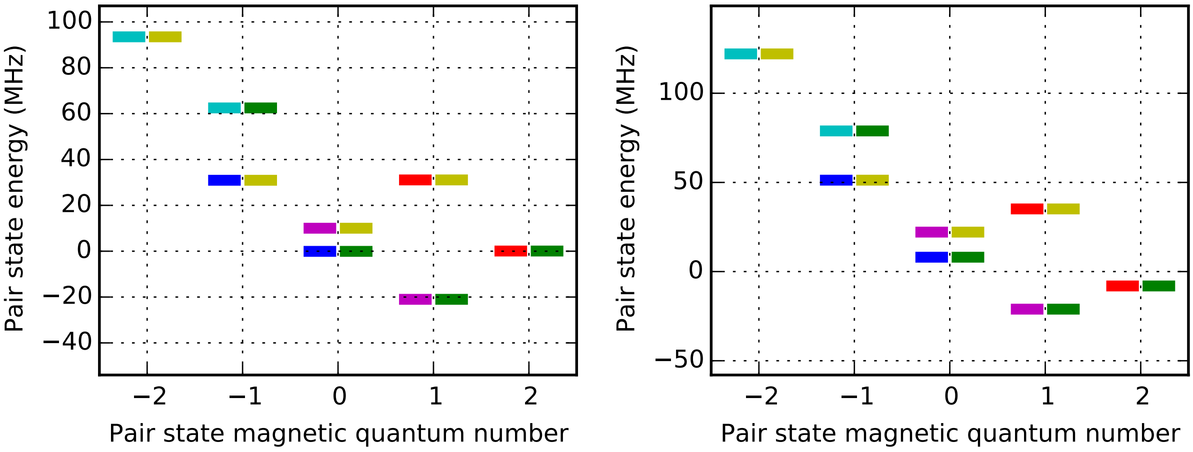

(a) Energies for $\mu = 0\,\mathrm{MHz}$ (using a magnetic field of $B = -11.2\,\mathrm{G}$).

(b) Energies for $\mu = -8\,\mathrm{MHz}$ (using a magnetic field of $B = -15.6\,\mathrm{G}$).

Fig. 3.2.: Pair state energies assuming that both atoms are in one of the states shown in 3.1. The energies are given for $\mu = 0\,\mathrm{MHz}$ (a) as well as for $\mu = -8\,\mathrm{MHz}$ (b), since we are going to use both of these values later on.

For $\mu = 0\,\mathrm{MHz}$, the pair states of the V scheme are degenerate and their energetic separation is larger than the interaction strengths. Thus, we can stay in the subspace of our V scheme.

For $\mu = -8\,\mathrm{MHz}$, the pair states of the V scheme are separated by $2 \cdot 8\,\mathrm{MHz}$. Now, the state colored in magenta-yellow ($|P_{m_J=1/2}, S_{m_J=-1/2}\rangle$, respectively $|S_{m_J=-1/2}, P_{m_J=1/2}\rangle$) could become important, too. However, we will use this scheme only if we excite to the $|+\rangle$ state. In this case, the coupling to magenta-yellow would be a second order process. Hence, we assume it to be negligible, so that we can stay in the subspace of our V scheme.

3.1. Triangle system with evidence for spin-orbit coupling

Before we start working on topologically non-trivial systems, we would like to investigate a simple triangle system for two reasons: First, the implementation of such a system could be used as a preliminary test before one starts to experimentally realize more complicated systems. Second, it is interesting by itself as we will see in the following.

Let us assume that the triangle is build from atoms in the $|0\rangle$ state with level structures as described above. Unlike later, we use $\mu = 0\,\mathrm{MHz}$ and an interatomic distance of $20\,\mu\mathrm{m}$ to get slow dynamics that can be nicely observed. Now, we initially excite on of the atoms into the $|+\rangle$ or $|-\rangle$ orbital. The resulting dynamics are shown in 3.3. Remarkably, the excitation propagates asymmetrically, despite the symmetric positioning of the atoms. The asymmetry originates from the spin-orbit coupling. It has the effect that excitations to the $|+\rangle$ and $|-\rangle$ states break the symmetry of the system. This can be understood as follows: We excite P_+ or P_- orbitals, that are not mirror symmetric. Instead, the P_+ orbital gets a P_- orbital under reflection and vice versa. Hence, if a model contains both types of orbitals and treats them differently, symmetries get broken. In our model, this is the case since P_+ and P_- orbitals collect opposite phases during hopping. Besides, t_+ is different from t_-. If we switch off the spin-orbit coupling (e.g. by setting $w = 0$ or using a very large value of μ such that excitations to $|+\rangle$ and $|-\rangle$ are energetically separated), the propagation is symmetric.

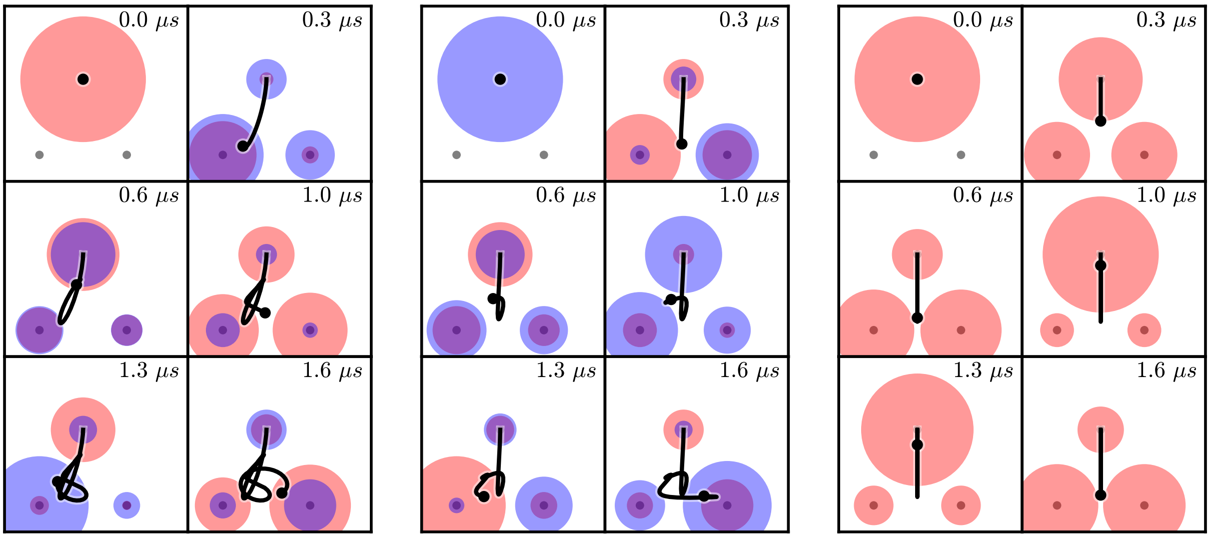

(a) With spin-orbit coupling, initial excitation to $|+\rangle$.

(b) With spin-orbit coupling, initial excitation to $|-\rangle$.

(c) Without spin-orbit coupling.

Fig. 3.3.: Time series of a hopping excitation in different triangle systems. Initially, one atom is excited to either $|+\rangle$ or $|-\rangle$. Since our dipolar model contains spin-orbit coupling, the propagation is asymmetric (a, b). For comparison, the propagation for zero spin-orbit coupling (c) is shown, too. The black line describes the center of mass movement of the excitation. The color of the bubbles indicates whether it is an excitation to $|+\rangle$ (red) or $|-\rangle$ (blue). Their size is proportional to the probability of finding the excitation.

3.2. Minimal system with topological bands

The aim of this section is to develop a minimal topological system that can be experimentally realized: Starting with an infinite system with topological bands, we consider smaller and smaller systems ensuring that they stay “topologically interesting”. Finally, we end up with a minimal system that shows edge states as a remnant of topological bands.

For this proposal, we use Rydberg atoms with the priorly described V level structure. We place the atoms in an infinite honeycomb lattice, since — in case of lattice boundaries — this geometry gives rise to energetically separated edge states that can be easily excited as we shell see later on. We choose the lattice constant to be $a = 10\,\mu$m. Further, we assume that one atom is excited to $|+\rangle$ and all the other atoms are in the $|0\rangle$ state. Using this setup with realistic tunneling strengths, we indeed obtain topological bands, see figure 3.4.

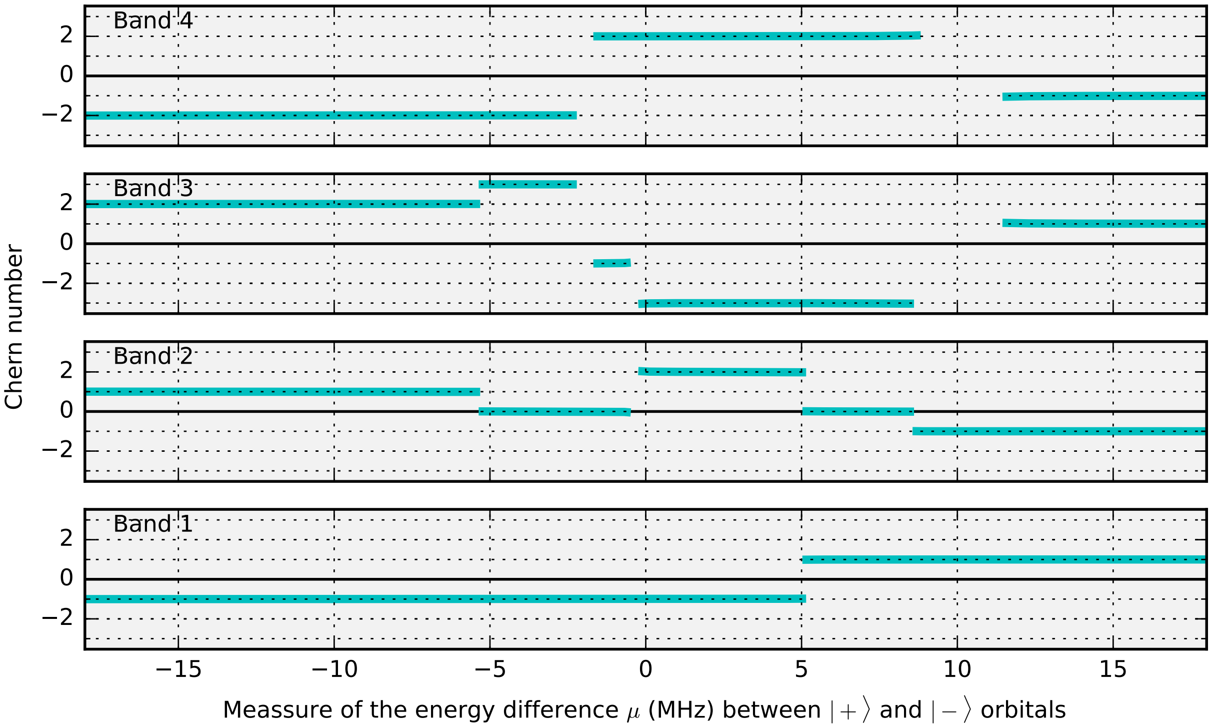

Fig. 3.4.: Topological phase diagram. The cyan colored lines show numerically calculated Chern numbers as functions of μ for our honeycomb system. If the Chern number is not defined because of band closings, no lines are drawn.

The Chern numbers of the four bands[1] of our honeycomb lattice are calculated as a function of the parameter μ that can be controlled through the fields. We see from this calculation that there are plenty of different phases. Since we would like to be in a region where the Chern number is stable, we use $\mu = -8\,$MHz in the remainder of this chapter. Here, the lowest band has a Chern number equal to -1 and the band above a Chern number equal

---

[1] We have four bands, since the honeycomb lattice has a two-atom basis and our model has two orbitals.

to +1. In case of boundaries, we expect as many edge states between these two bands as there are edges in the system. The small value of μ is useful for a second reason, too: It ensures that the two lower bands of the band structure mainly consist of the $|+\rangle$ orbital, see figure 3.5. The same will apply to edge states between these two bands, so that they can be simply probed by an excitation to the $|+\rangle$ state.

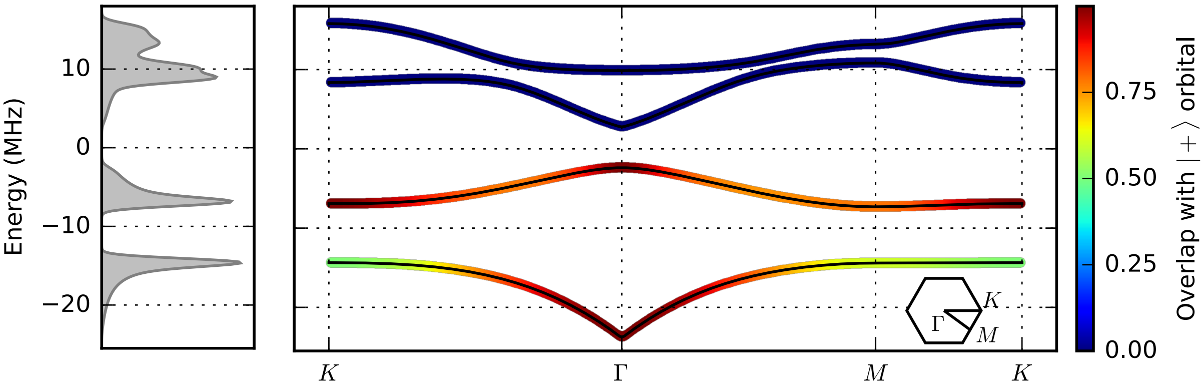

Fig. 3.5.: Band structure of an infinite honeycomb system, plotted along a path through high symmetry points of the Brillouin zone. The color shows the overlap between the states of the band structure and the $|+\rangle$ orbital.

Having the infinite honeycomb lattice, we can study the dynamics of bulk excitations. Two examples are shown in figure 3.6.

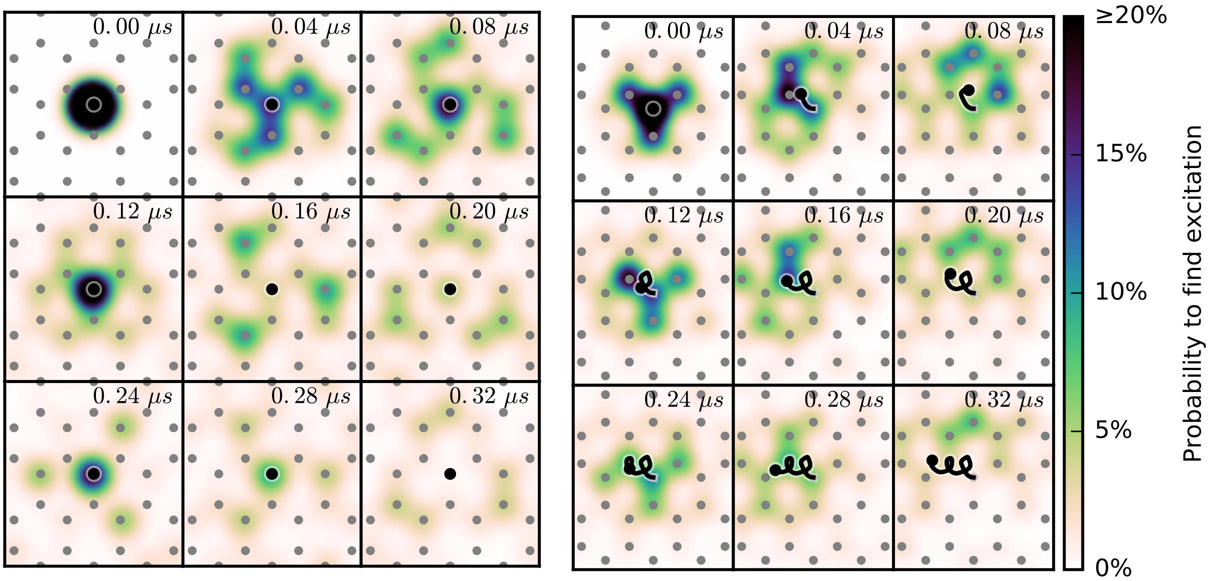

(a) Excitation of one single atom.

(b) Gaussian excitation distributed over several atoms. Initial velocity to the left.

Fig. 3.6.: Propagation of bulk excitations in an infinite honeycomb system. The color code shows the probability to find an excitation and the black line indicates the excitation's center of mass movement.

If an excitation is located at one single lattice site, it spreads anisotropically, showing a rotational structure. This asymmetry is a result of the spin-orbit coupling. If an excitation is distributed over several lattice sites, we can give it a velocity. In this case, the excitation performs movements that remind on the drift motion of electrons in magnetic fields. This shows the relation to quantum Hall physics.

Edge states in a half-finite system

Now, we would like to investigate half-finite systems. Here, we get edge states on the boundaries due to topological bands. The edge states cross the band gaps as it is shown in figure 3.7. In order to highlight the edge states inside the band structure, we color the states according to their expectation value of the lateral position measured from the center of the half-finite lattice.

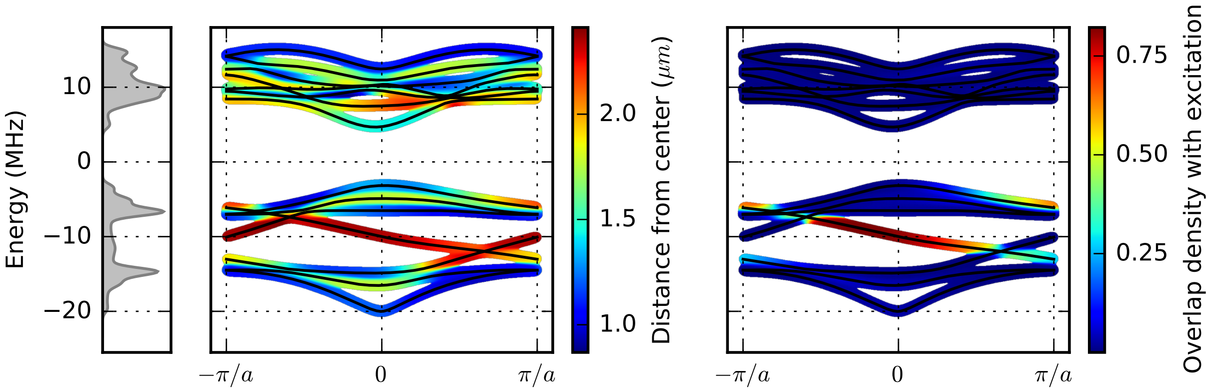

Fig. 3.7.: Band structure of a half-finite honeycomb system. The plot besides the density of states visualizes whether band structure states live at the edge (red) or in the bulk (blue). For this visualization, we calculated the expectation values of the lateral position measured from the center of the half-finite lattice. The right plot shows their overlap with an excitation to the $|+\rangle$ orbital at the armchair edge, see figure 3.8.

There are two distinct edge states because of the two boundaries of the half-finite system. We try to excite the edge state that belongs to the armchair edge since it is more pronounced. For this we place one excitation in the $|+\rangle$ orbital on this edge. The overlap between this excitation and the states of the band structure is shown in figure 3.7. As we can see, the excitation works very well. This impression is reinforced by the propagation of the edge excitation, see figure 3.8: It perpetually stays at the edge. The center of mass movement reminds of skipping orbits. This demonstrates again the relation to quantum Hall physics. For comparison, we show what would happen in a topologically trivial system[2], where the excitation would just propagate into the bulk.

---

[2] A topologically trivial system can be realized using a huge value for μ. Then, the $|+\rangle$ and $|-\rangle$ orbitals are separated by a great difference in energy so that they can not couple anymore.

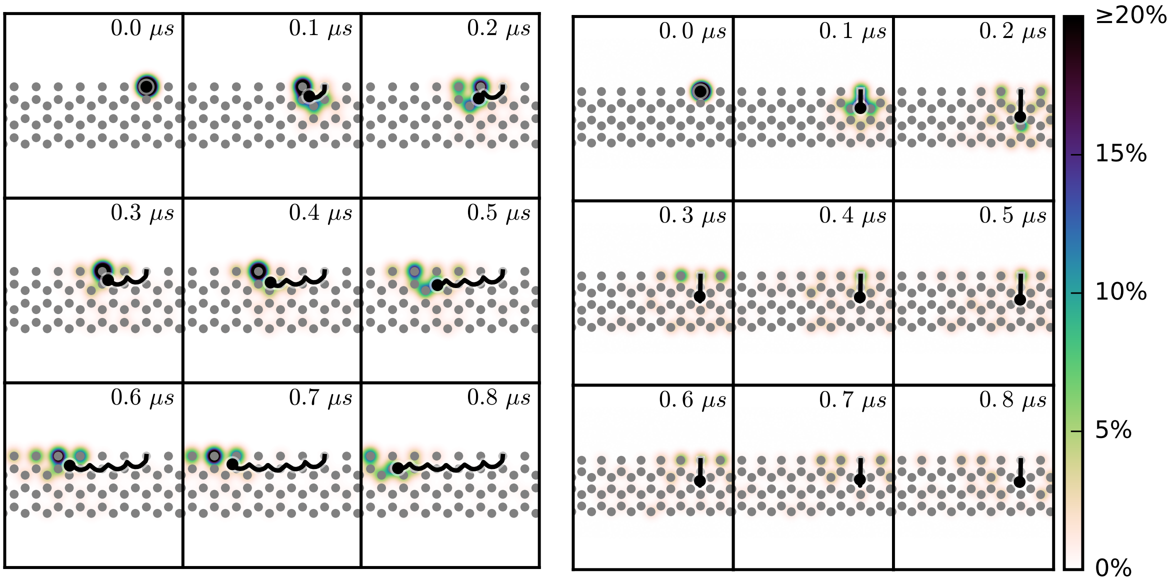

(a) Our system with topological bands. *(b)* Topologically trivial system.

Fig. 3.8.: Propagation of an edge excitation to the $|+\rangle$ orbital in a half-finite honeycomb system. In our case, the excitation propagates along the edge. In case of a topologically trivial system, the excitation spreads into the bulk.

Edge states in a large disk-shaped system

Since only completely finite systems can be realized in the laboratory, we study the edge state propagation on a disk-shaped honeycomb system with 31 atoms. A “normal” band structure can not be calculated for it due to its finite size. Here, we can make use of our newly developed unwrapped band structure. It is shown in figure 3.9.

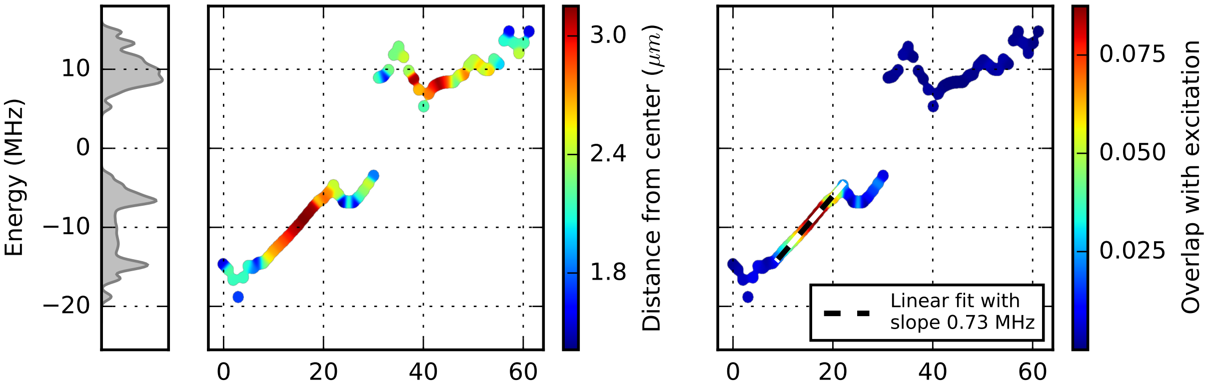

Fig. 3.9.: Unwrapped band structure of a disk-shaped honeycomb system with 31 atoms. The location of the states is calculated as the expectation values of the radial coordinate. The two lower bulk bands, that are visible as little peaks, are connected with an edge state (colored in red) as it was the case in the half-finite system.

The two lower bulk bands are still visible as little peaks. One state[3] with a linear dispersion is located between them. Its red color proves that this state is indeed an edge state. From its dispersion relation, we can determine the group velocity in the usual way: $v = \frac{\partial \omega}{\partial m} = 0.72\,\mathrm{MHz}$. The dimension of this velocity has to be interpreted as a rotation frequency. The real propagation of the excitation (see figure 3.2) is in great agreement with this result. All this demonstrates impressively that there is no fundamental difference between our disk-shaped system and the previously investigated half-finite system.

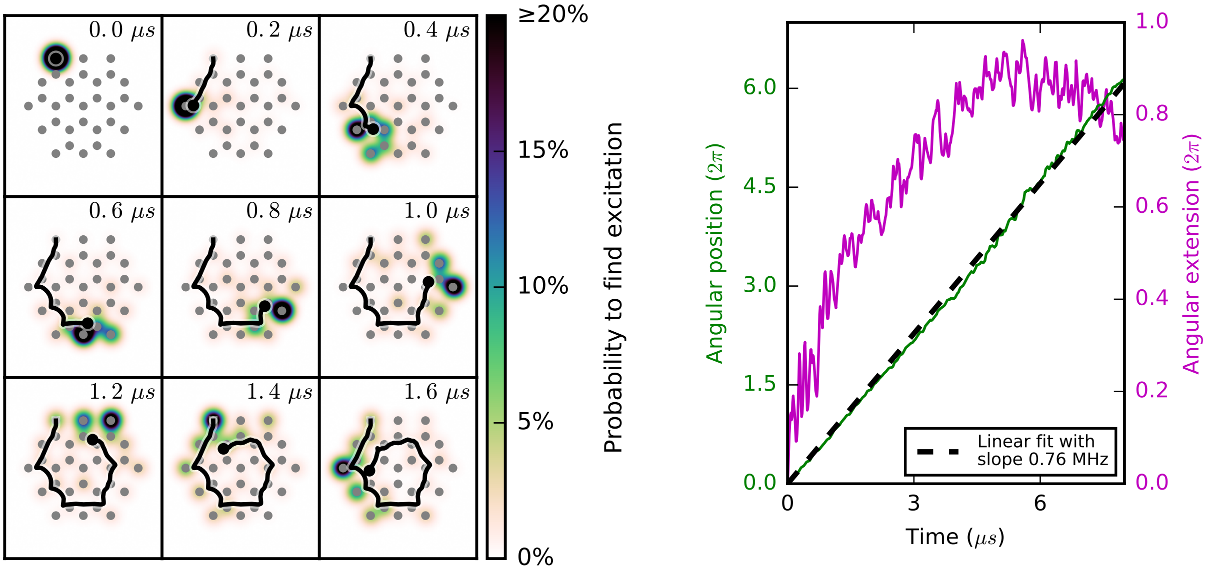

(a) Hopping of edge excitation.

(b) Angular position and extension of edge excitation as a function of time.

Fig. 3.10.: Propagation of an edge excitation to the $|+\rangle$ orbital in a disk-shaped system with 31 atoms. The angular movement of the center of mass can be traced for several rounds.

Since the dispersion is not perfectly linear, the angular extension of the excitation gets larger in time. To describe this behavior quantitatively, we define a measure of the angular extension: Let us introduce the variable α that describes angles under which the excitation can be found. The polar angle of the center of mass of the excitation is named φ_{COM}. Using these quantities, we can define the angular extension as the expectation value $\langle|\varphi_{\mathrm{COM}} - \alpha|\rangle \cdot 4$. The factor of 4 enables an easy interpretation of our measure: It is 2π if an excitation is homogeneously spread over the edge of a disk-shaped system.

Edge states in a small disk-shaped system

At the time of writing, our system with 31 atoms is still too big to be realized. Thus, we search for smaller systems that show remnants of topological bands. The smallest system

---

[3] We have only one edge state since there is only one boundary — and not two as in the case of the half-finite system.

we found has 10 atoms and is as such not far from experimental realization. Its unwrapped band structure is shown in figure 3.11.

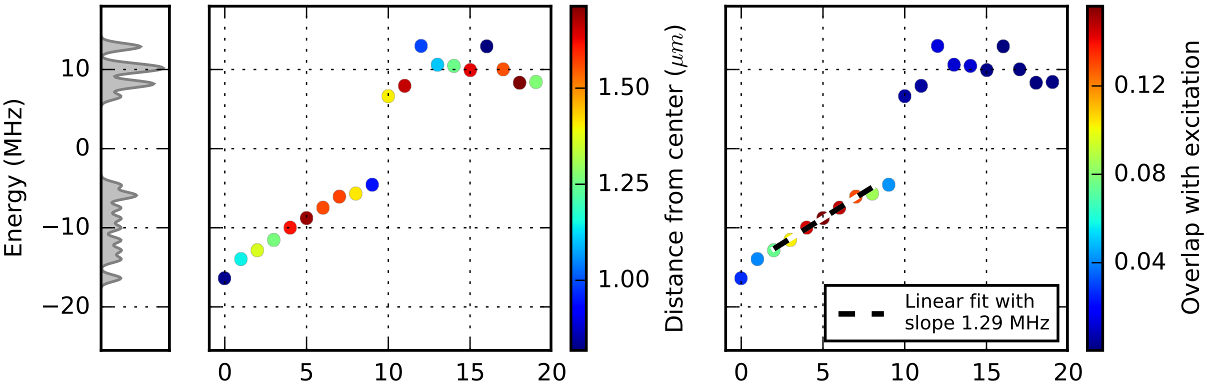

Fig. 3.11.: Unwrapped band structure of a disk-shaped honeycomb system with 10 atoms.

Although the unwrapped band structure no longer contains much information, we can still let an excitation nicely propagate along the edge as it is shown in figure 3.2. Even the velocity of propagation is still in agreement with the group velocity taken from the unwrapped band structure. All in all we can conclude, that the edge state as remnant of topological bands is still present in this very small system and that it can be experimentally probed with an excitation into the $|+\rangle$ orbital.

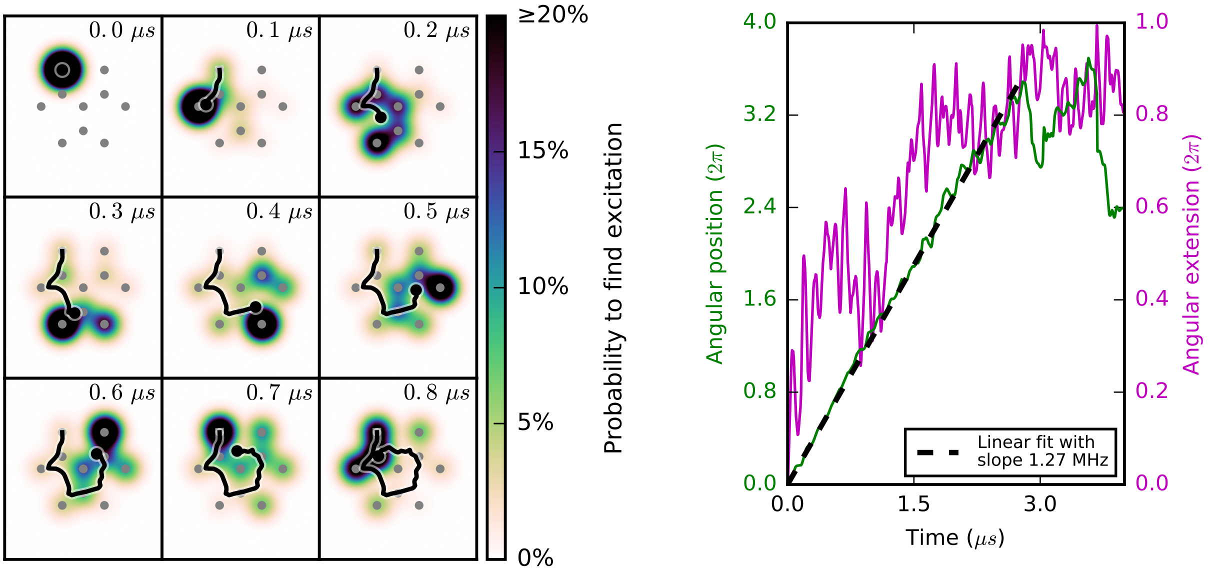

(a) Hopping of edge excitation.

(b) Angular position and extension of edge excitation as a function of time.

Fig. 3.12.: Propagation of an edge excitation to the $|+\rangle$ orbital in a disk-shaped system with 10 atoms. The propagation can be traced for three rounds. Afterwards, the excitation is distributed over the whole edge as the plot of the angular extension shows.

3.3. Robustness to lattice defects

For the experimental realization it is an important question how robust to lattice defects the edge state propagation is. To answer this question, we add Gaussian noise with a standard deviation between 5 % and 10 % of the lattice constant to the positions of the lattice sites. The averaged results, that are shown in figure 3.13, indicate that a disorder of 5 % is still tolerable whereas a disorder of 10 % is too large.

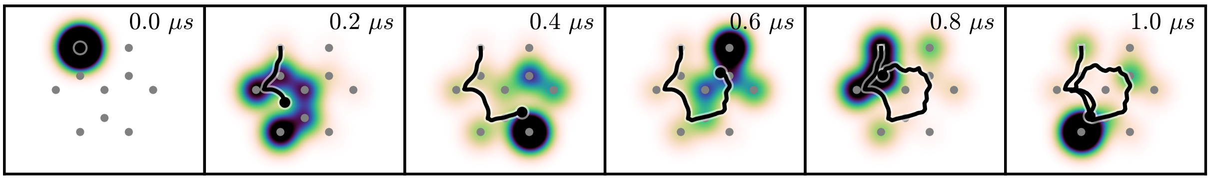

(a) No lattice disorder.

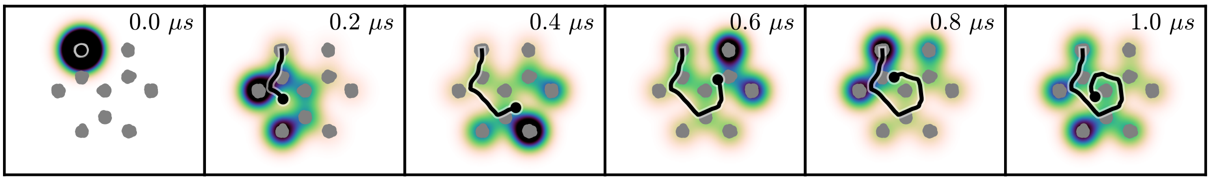

(b) Gaussian disorder with standard deviation equal to 5 % of the lattice constant.

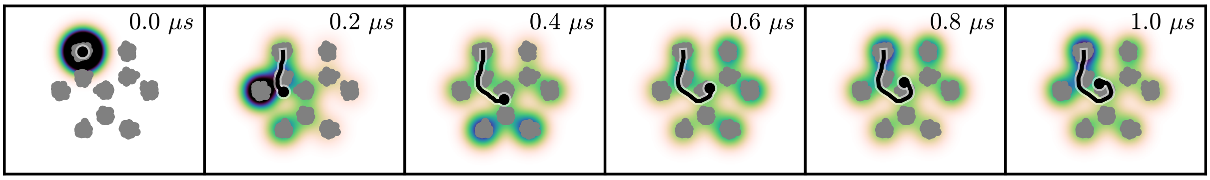

(c) Gaussian disorder with standard deviation equal to 10 % of the lattice constant.

Fig. 3.13.: Influence of lattice disorder on the propagation of an edge excitation. Plots averaged over 100 runs. Same color code as in the previous plots.

Instead of implementing the minimal system, one can also realize a larger system if a partial loading of the lattice is acceptable. In order to find out which loading is needed at least, we simulate the edge state propagation on our system with 31 lattice sites in case of added lattice vacancies. Figure 3.14 shows results averaged over 100 runs. At a vacancy probability of 13 % we still nicely see the propagation of the edge excitation. Actually, it works even better than the figure suggests: Atoms removed from the boundary of the system do not necessarily make the system topologically trivial, but the edge state is unavoidably modified and the excitation has to go a slightly different way. If one averages over several plots, this effect makes the propagation appear worse than it really is. Thus, we could perhaps get better results with more sophisticated analyzations. At a vacancy density of 26 % the edge state starts to vanish. This result is in good agreement with the sample averaged Chern number that begins to drop to zero at this vacancy density, see figure 4.2. The sample averaged Chern number is calculated using infinite systems with enlarged unit cells obtained by repeating the two-atom unit cell of the honeycomb lattice along each lattice vector (e.g. in our case for seven times). From this big unit cells atoms are randomly removed according to the vacancy probability. Because of the enlarged unit cell many bands exist. To get the Chern number of the lowest band of our original system, we sum up the Chern numbers of the quarter of the bands with lowest energy.

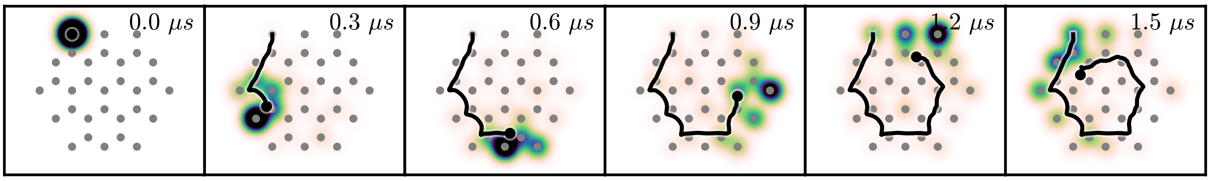

(a) No vacancies.

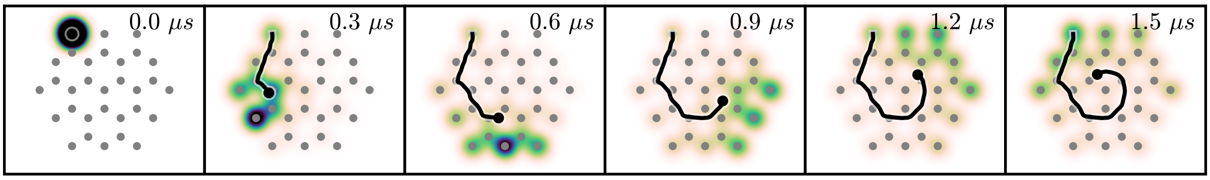

(b) Vacancy probability of 13 %.

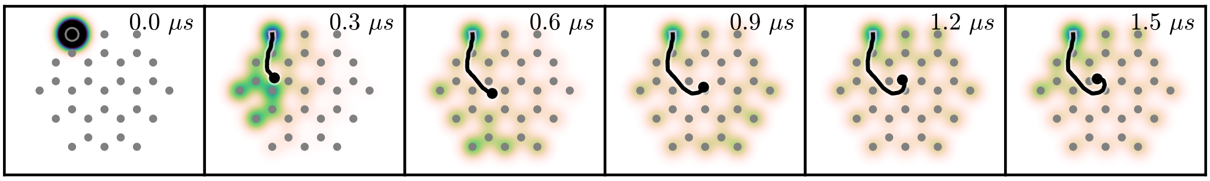

(c) Vacancy probability of 26 %.

Fig. 3.14.: Influence of lattice vacancies on the propagation of an edge excitation. Plots averaged over 100 runs. Same color code as in the previous plots.

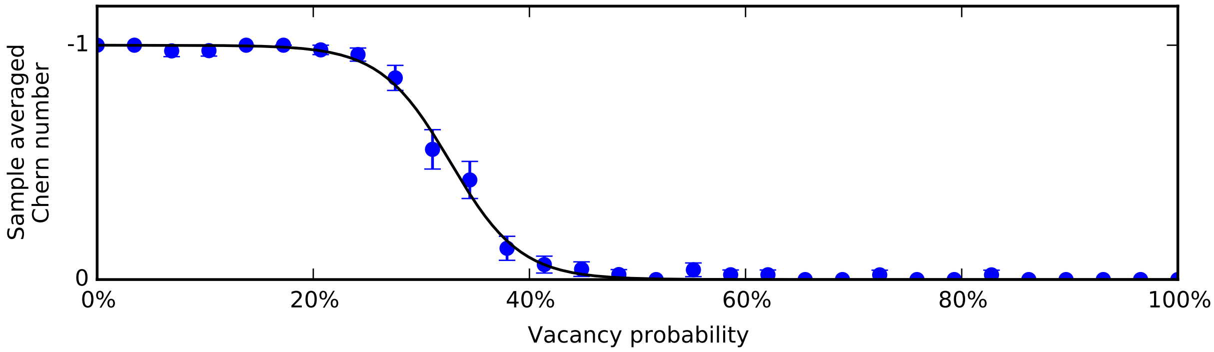

Fig. 3.15.: Sample averaged Chern number of the lowest band as a function of the vacancy density. The black line serves as a guide to the eye.

These calculations indicate that vacancy probabilities below $\sim 20\,\%$ are acceptable. The robustness comes on the one hand from the fact that topology is a non-local property and on the other hand from the long-ranging dipolar interaction that bridges some vacancies.

4. Interaction potentials with short distance cutoffs

4.1. Increased robustness

Since a loading of 80 % is still hard to achieve, we would like to increase the robustness. Our goal is to get a tolerable vacancy probability of 50 % because then one can use probabilistic lattice loading schemes as in [26]. With very robust topological bands, experiments might be possible in atomic clouds, too.

The key observation for making topological bands more robust is, that lattice defects cause small scale variations. If we zoom out or blur our lattice, they are not present anymore. Unfortunately, in the case of the dipolar potential $1/|R_{ij}|^3$, the nearest neighbor sites have a very high impact so that small scale variations are seen very well from our model. Hence, we need to modify our interaction potential with a short-distance cutoff. Experimentally, this might be done using the Rydberg blockade[1]. The idea is that the effective interaction of Rydberg dressed atoms [28] or Rydberg polaritons [29] can be described via cutoff potentials.

It turns out that cutoff potentials work best if they completely suppress nearest neighbor interaction, but for a distinct increase of robustness already a slight suppression is enough. Since the actual form of the potential is not crucial, we can model it by the following equation:

$$V_s(R) = c_s \cdot \frac{R^9}{(R^6 + s^6/3)^2}, \tag{4.1}$$

where c_s is a normalization constant. It is chosen in such a way that the potential energy summed over all lattice sites is equal to the total potential energy that we would obtain in case of an ordinary dipolar interaction. The shift parameter s determines the position of the maximum of the cutoff potential. For s equal to zero, we obtain the standard dipolar potential. The tail of our cutoff potential is given by the dipolar potential and its short distance behavior is motivated by the Rydberg blockade.

Figure 4.1 shows the cutoff potentials of different shifts. For better visibility, they are not normalized as described above — instead their energies are scaled in such a way that their maximum value is one. The triangle markers show energies that occurs in a square lattice (thus, the markers at $|R_{ij}|/a = 1$ represent the nearest neighbor interaction energies).

---

[1] Current research on the realization of cutoff potentials is done by my colleague Przemek Bienias

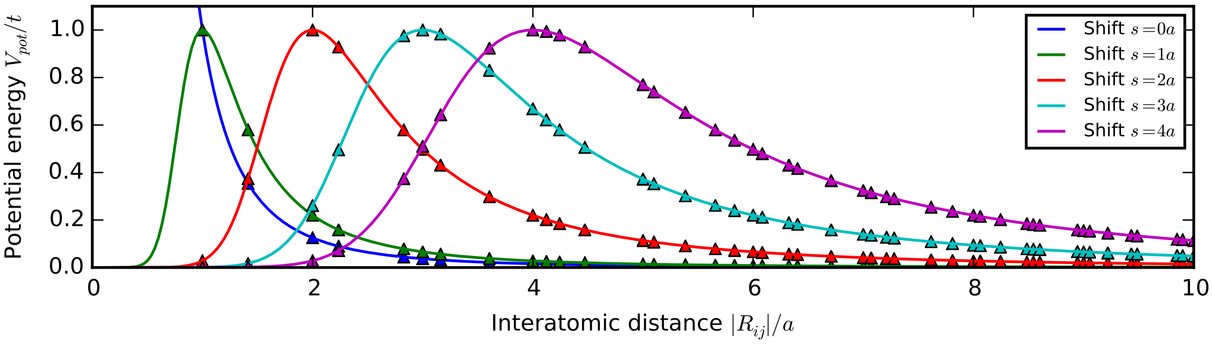

Fig. 4.1.: Visualization of cutoff-potentials. For better visibility, the energies are scaled such that their maximum value is one. Triangle markers show energies in a square lattice.

In this chapter, we use a square lattice system since it has only two bands so that the interpretation of the results is easier than for the honeycomb lattice[2]. For this system we specify the parameters as follows: $(t^- + t^+)/2 = 0$, $(t^- - t^+)/2 = t$, $w = 3t$, and $\mu = -3t$ (different parameters would also work as long as one stays in a topological phase). Figure 4.1 depicts the sample averaged Chern number[3] as a function of the vacancy probability for the cutoff potentials shown in 4.1.

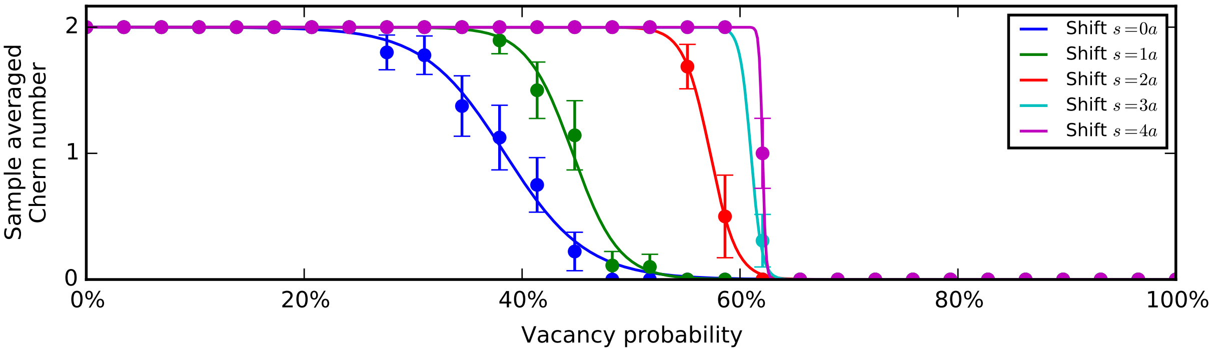

Fig. 4.2.: Sample averaged Chern number as a function of the vacancy density. The solid lines serve as a guide to the eye. In case of moderate vacancy probabilities, the Chern number is two since we are in a square lattice.

This figure tells us that we can nearly double the robustness to vacancies using cutoff potentials. Even a slight change of the ratio between nearest neighbor interaction and other interaction energies leads to a significant change in robustness (green). As soon as nearest neighbor interaction is completely suppressed, the topological bands are much more stable (red).

---

[2] In the next section we try to connect numerical results for cutoff potentials to analytic results for a continuum model. In order to do this for the honeycomb lattice, we would have to add the Chern numbers of the lower respectively upper bands together to obtain an effective two band model.

[3] For a two-band system we get all information about its topology by plotting the Chern number of one single band. The Chern number of the other band is equal to its negative value.

4.2. Approaching the continuum limit

Cutoff potentials are impressive for a second reason, too: Let us imagine that the interaction potential acts on length scales larger than the lattice constant. Then, the lattice is not seen by the potential at all. Hence, we can approximate such a system with a continuum model. We obtain it by starting with a square lattice and taking the limit $a/s \to 0$. In the discrete case, position and momentum space are linked by the discrete Fourier transform 1.17. In the continuum, it gets

$$\boldsymbol{\psi}(\boldsymbol{r}) = \frac{1}{\sqrt{2\pi}} \int_{\mathbb{R}^2} \mathrm{d}\boldsymbol{k}\ \boldsymbol{\psi}(\boldsymbol{k})\ \mathrm{e}^{\mathrm{i}\boldsymbol{k}\boldsymbol{r}}. \tag{4.2}$$

Using this equation we can do the same calculations as in section 1.4 of the introduction and end up with a continuum analogue of equation 1.25:

$$\begin{aligned}
\epsilon^m(\boldsymbol{k}) &= \int_{\mathbb{R}^2} \mathrm{d}\boldsymbol{r}\ V_s(r)\ \mathrm{e}^{\mathrm{i}m\phi}\mathrm{e}^{\mathrm{i}\boldsymbol{k}\boldsymbol{r}} \\
&= \int_0^\infty \mathrm{d}r \int_0^{2\pi} \mathrm{d}\phi\ V_s(r)\ r\ \mathrm{e}^{\mathrm{i}m\phi}\mathrm{e}^{\mathrm{i}kr\cos(\phi-\angle\boldsymbol{k})} \\
&= (-1)^m \int_0^\infty \mathrm{d}r \int_{-\pi}^{\pi} \mathrm{d}\phi\ V_s(r)\ r\ \mathrm{e}^{\mathrm{i}m\phi}\mathrm{e}^{-\mathrm{i}kr\sin(\phi-\angle\boldsymbol{k})} \qquad (4.3)\\
&= (-1)^m\ \mathrm{e}^{\mathrm{i}m\angle\boldsymbol{k}} \int_0^\infty \mathrm{d}r \int_{-\pi-\angle\boldsymbol{k}}^{\pi-\angle\boldsymbol{k}} \mathrm{d}\phi\ V_s(r)\ r\ \mathrm{e}^{\mathrm{i}m\phi}\mathrm{e}^{-\mathrm{i}kr\sin(\phi)}. \qquad (4.4)
\end{aligned}$$

where V_s is the cutoff potential and $\angle\boldsymbol{k}$ denotes the polar angle of $\boldsymbol{k}$. Since $\mathrm{e}^{\mathrm{i}m\phi}\mathrm{e}^{-\mathrm{i}kr\sin(\phi)}$ is a 2π-periodic function because of the integer valued m, we can integrate from $-\pi$ to π and identify the Bessel function of the first kind:

$$J_m(x) = \frac{1}{2\pi} \int_{-\pi}^{\pi} \mathrm{d}\phi\ \mathrm{e}^{\mathrm{i}m\phi}\mathrm{e}^{-\mathrm{i}x\sin\phi}. \tag{4.5}$$

We obtain

$$\begin{aligned}
\epsilon^m(\boldsymbol{k}) &= 2\pi\ (-1)^m\ \mathrm{e}^{\mathrm{i}m\angle\boldsymbol{k}} \int_0^\infty \mathrm{d}r\ V_s(r)\ r\ J_m(kr) \\
&= 2\pi\ (-1)^m\ \mathrm{e}^{\mathrm{i}m\angle\boldsymbol{k}} F_m(k) \equiv \mathrm{e}^{\mathrm{i}m\angle\boldsymbol{k}} W_m(k), \qquad (4.6)
\end{aligned}$$

where $F_m(k)$ is the Hankel transform of the cutoff potential. We can use this expression to determine the $\boldsymbol{n}$-vector 1.24:

$$\boldsymbol{n}(\boldsymbol{k}) = \begin{pmatrix} w\ \mathrm{Re}\ \epsilon^2(\boldsymbol{k}) \\ w\ \mathrm{Im}\ \epsilon^2(\boldsymbol{k}) \\ \mu + t\epsilon^0\boldsymbol{k} \end{pmatrix} = \begin{pmatrix} w\ \cos(2\angle\boldsymbol{k})\ W_2(k) \\ w\ \sin(2\angle\boldsymbol{k})\ W_2(k) \\ \mu + tW_0(k) \end{pmatrix} = R_z(2\angle\boldsymbol{k}) \begin{pmatrix} w\ W_2(k) \\ 0 \\ \mu + tW_0(k) \end{pmatrix}, \tag{4.7}$$

where $R_z(2\angle\boldsymbol{k})$ is a rotation around the Z-axis by the angle $2\angle\boldsymbol{k}$. This result allows us to calculate the Chern number of our continuum model via equation 1.9

$$C = \frac{1}{4\pi} \int_{\mathbb{R}^2} \mathrm{d}^2\boldsymbol{k}\ (\partial_{k_x}\hat{\boldsymbol{n}}(\boldsymbol{k}) \times \partial_{k_y}\hat{\boldsymbol{n}}(\boldsymbol{k})) \cdot \hat{\boldsymbol{n}}(\boldsymbol{k}), \tag{4.8}$$

where we have replaced the integration over the Brillouin zone by the integral over $\mathbb{R}^2$ because of the continuum. To evaluate this expression we apply a trick:

Since $J_m(x)$ tends to zero like $1/\sqrt{x}$ for x to infinity [30], it holds $\epsilon^m(|\boldsymbol{k}| \to \infty) = 0$ (at least for our nicely behaving potentials). Thus, $\hat{\boldsymbol{n}} = \boldsymbol{n}/|\boldsymbol{n}| = (0, 0, \text{sign}(\mu))^T$ is the same for all points at infinity and we can compactify $\mathbb{R}^2$ into a sphere S^2. This allows us to identify the integral 4.8 as winding number[4]. Hence, we do not need to evaluate it explicitly. All we have to do is to count how often $\hat{\boldsymbol{n}}(\boldsymbol{k})$ winds around the unit sphere as we integrate over S^2.

The rotation matrix $R_z(2\angle\boldsymbol{k})$ from equation 4.7 makes the vector $\hat{\boldsymbol{n}}$ rotate around the Z-axis for two times. Further, we know from above that $\hat{\boldsymbol{n}}(\infty)$ points in the direction of $(0, 0, \mu)^T$. Since $J_2(0)$ is equal to zero and $J_0(0)$ is equal to one, $\hat{\boldsymbol{n}}(0)$ points in the direction of $(0, 0, \mu + t\epsilon^0(0))^T$. If these two directions are opposed, we have a winding number of two[5].

These considerations give us the boundaries of the topological phases: We have phase transitions at $\mu = 0$ and $\mu/t = -\epsilon^0(0)$[6]. In-between, there is a phase with a Chern number of two. Figure 4.3 compares this analytic result for the continuum model to numerical calculations for cutoff potentials.

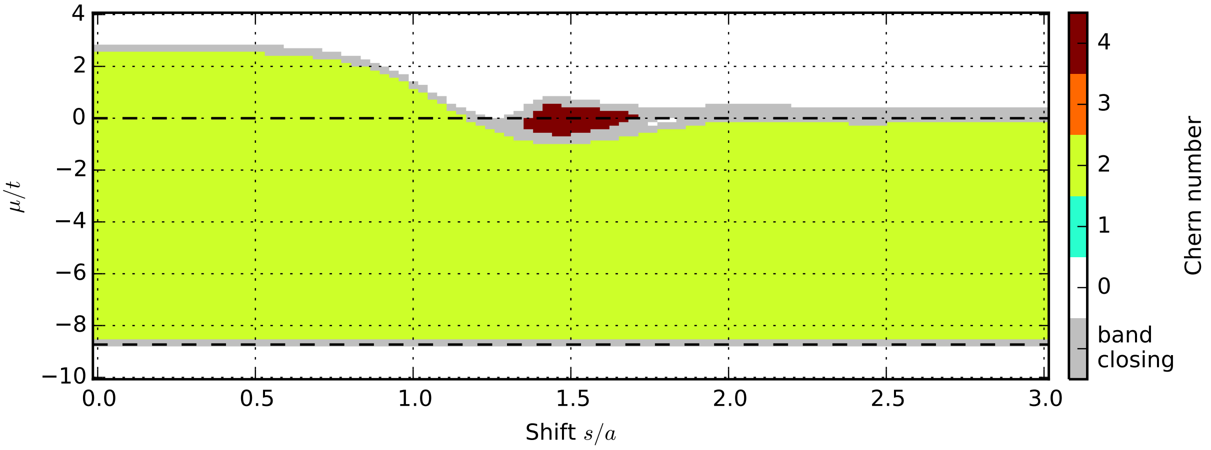

Fig. 4.3.: The colormap shows the topological phases for systems with cutoff potentials. The dotted lines represent the phase boundaries of our continuum model. This figure proves that the we rapidly approach the continuum limit if we increase the shift.

It shows that we approach the continuum limit if we increase the shift. Already for a shift of 2 a, the cutoff system exhibits a phase diagram very similar to the one of the continuum model. The good agreement at this value is no coincidence: Here, the nearest neighbor

---

[4] This is the same trick that it is commonly done for skyrmions.

[5] The winding number could be even higher if $\hat{\boldsymbol{n}}$ flipped around for intermediate values of $\boldsymbol{k}$. However, numerical results prove that this is not the case for our potentials.

[6] We choose the normalization of the cutoff potential so that $\epsilon^0(0)$ assumes the value that we would obtain for the dipolar model on a square lattice.

interaction is completely suppressed as we have seen before. It is also worth mentioning that we obtain an additional phase with a Chern number of four at a shift of 1.5 a.

In figure 4.4 we show the band closings at the phase boundaries. The band structures are calculated for the continuum model[7]. The closings happen for large values of k and for $k = 0$. If we compare this band structures to the dipolar model on a square lattice as it was presented in [6], the following correspondences get obvious: $k = \infty$ corresponds to the M point whereas $k = 0$ corresponds to the Γ point of Brillouin zone of a square lattice. The Chern numbers match, too. Hence, we have obtained a continuum model that shows similar physics as the dipolar model on the square lattice and is a such fundamentally different to the quantum Hall effect.

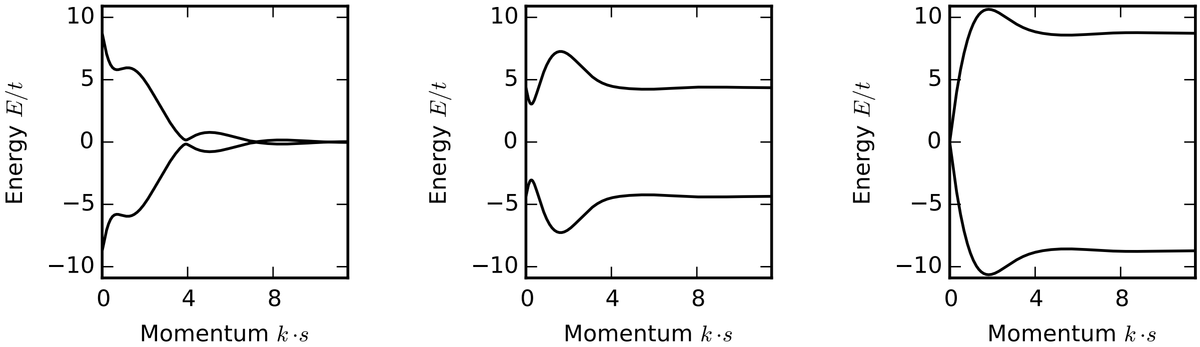

(a) Continuum band structure at $\mu/t = 0$.

(b) Continuum band structure at $\mu/t = -4.36$.

(c) Continuum band structure at $\mu/t = -8.73$.

Fig. 4.4.: Band structures of the continuum model calculated at phase boundaries as well as in the middel of the Chern 2 phase (see figure 4.3). One clearly sees the band touchings that appear in case of phase transitions.

---

[7] In the continuum model, moments can in principle assume arbitrary high values. However, interesting physics happen only at moments comparable to the reciprocal value of the shift s which is the characteristic length scale of the continuum system.

5. Conclusion and outlook

At the beginning of this thesis, we developed a band structure analogue for finite systems that allows us to obtain the number of edge states as well as their dispersion in finite systems. It works reliable for different models and arbitrary lattice geometries.

After this theoretical groundwork, we presented a proposal on how to experimentally realize topological bands using the dipolar interaction of Rydberg atoms. We placed great emphasis on using realistic parameters. They support topologically non-trivial phases, that give rise to edge states in case of lattice boundaries. We showed that one can probe the edge states by exciting one atom at the boundary and by observing the propagation of the excitation. Starting from a half-finite system, we demonstrated that this works in systems with as few as ten atoms. Our newly developed band structure analogue helped us to ensure that the edge states of the half-finite system survived the reduction of the system size. Furthermore, we showed that the existence of edge states is robust against lattice defects. All this makes us confident that topological bands are indeed experimentally feasible using the dipolar interaction of Rydberg atoms.

In the last part, we studied the effect of cutoff potentials that might be realizable via the Rydberg blockade. Cutoff potentials can be used to dramatically increase the robustness to lattice defects as well as to realize a continuum-like model whose topological phase diagram can be calculated analytically. It shows that topological bands in the continuum can originate from other phenomena than the quantum Hall effect, too.

Our plan for the future is to search for many-body effects in these systems via exact diagonalization. Since we can tune parameters to obtain flat bands, we hope to find states with fractional excitations (like in the fractional quantum Hall effect). This might give us new insights into the nature of interesting many-body states with topological order that are not fully understood, yet. Perhaps such states can be experimentally realized. In order to do so it would be essential to keep the system cold. In this regard, our approach for topological bands might be superior to many other techniques since it does not rely on lattice shaking or AC fields that can cause heating. Our ultimative goal would be to extend the proposal presented in this thesis to an experimentally feasible system that give rise to interesting many-body ground states.

A. Atomic units

We would like to use a unit system that simplifies calculations in atomic physics. Furthermore, the units should be constructed in such a way that the quantities we deal with are of order one. This point is especially important for calculations with computers since too small or too large numbers can cause numerical errors.

A unit system that fulfills our demands is the system of Hartree atomic units [31, 32], in short: “atomic units”. It has the following appealing properties: Many constants of atomic physics are set to unity, immediately simplifying a lot of expressions. Furthermore, quantities related to the electron in the hydrogen ground state are of order one and hence well suited for numerical calculations.

Atomic units form a system of natural units and are as such grounded on universal physical constants. As it is shown in table A.1, the basic units are given by the four fundamental constants electron mass m_e, elementary charge e, reduced Planck's constant $\hbar$, and Coulomb's constant k_e. Their values in atomic units equal one by definition. Other units has to be derived. The most important ones are given in table A.2.

In general, we can write quantities as multiples of the fundamental constants given above, e.g. $1836\,\mathrm{m_e}$ for the proton mass. Since the constants are unity by definition we can omit them. In this case, it is common to put the label “a.u.” after a quantity to indicate that it is expressed in atomic units. Then, the quantity's dimension has to be inferred from the context.

Fundamental units

Dimension	Constant	SI value
mass	electron mass m_e	$9.10938291(40) \cdot 10^{-31}\,\mathrm{kg}$
charge	elementary charge e	$1.602176565(35) \cdot 10^{-19}\,\mathrm{C}$
action	reduced Planck's constant $\hbar$	$1.054571726(47) \cdot 10^{-34}\,\mathrm{J \cdot s}$
electric constant^{-1}	Coulomb's constant $k_\mathrm{e} = 1/(4\pi\epsilon_0)$	$8.9875517873681 \cdot 10^{9}\,\frac{\mathrm{kg \cdot m^3}}{\mathrm{s^2 \cdot C^2}}$

Tab. A.1.: The table shows the four fundamental constants that are the basis of atomic units. In SI units, their values are given in the table. In atomic units, they are all unity by definition. We can use this table to convert quantities having the same dimensions as the fundamental constants from SI to atomic units.

Derived units

Units related to magnetism can be defined in different ways. We have to settle what holds for a planar light wave in vacuum: $|E| = c|B|$ (SI like atomic units) or $|E| = |B|$ (Gaussian like atomic units). We decide to use the former convention.

Dimension	Constant	SI value
length	Bohr radius $a_0 = \hbar/(m_e c\alpha)$	$5.2917721092(17) \cdot 10^{-11}\,\mathrm{m}$
energy	Hartree energy $E_h = \alpha^2 m_e c^2$	$4.35974417(75) \cdot 10^{-18}\,\mathrm{J}$
time	period of classical electron in first Bohr orbit: $\hbar/E_h$	$2.418884326505(16) \cdot 10^{-17}\,\mathrm{s}$
electric field	field at distance a_0 from an elementary charge: $E_h/(ea_0)$	$5.14220652(11) \cdot 10^{11}\,\mathrm{V} \cdot \mathrm{m}^{-1}$
electric dipole moment	dipole moment of electron separated from proton by a_0: ea_0	$8.47835326(19) \cdot 10^{-30}\,\mathrm{C} \cdot \mathrm{m}$
magnetic field	$\hbar/(ea_0^2)$	$2.350517 \cdot 10^5\,\mathrm{T}$

Tab. A.2.: The table contains constants derived from the four fundamental constants given in table A.1. In atomic units their values are all unity as it can be shown by quick calculations. Quantities of the same dimension as the derived constants can be converted from SI to atomic units via this table. α is the fine-structure constant.

Important constants

Many constants that we will need — like the electron charge — are contained in tables A.1 and A.2 since their values are unity in atomic units. Of course this is not true for all constants. In the following we list other important constants.

Constant	Value in atomic units
Bohr magneton $\mu_B = e\hbar/(2m_e)$	$1/2\,\mathrm{a.u.}$
fine-structure constant α (the same in all unit systems because dimensionless)	$7.2973525664(17) \cdot 10^{-3} \approx 1/137$

Tab. A.3.: Important constants whose values are not unity in atomic units.

B. Matrix elements

We are interested in the interaction of atoms among each other or with electromagnetic fields. To get quantitative results, we have to evaluate matrix elements of operators. In order to obtain equations for matrix elements that are valid for various different operators, it is common to write them in terms of spherical tensors since many operators are combinations of them. A spherical tensor T_{kq} can be pictured as a spherical harmonic $Y_{l=k}^{m=q}$. A detailed discussion of spherical tensors can be found in chapter 4.3 of "Atomic Spectra and Radiative Transitions" by I. Sobelman [33]. Unless stated otherwise, the given formulas are taken from this book.

Wigner-Eckart theorem

All the following equations for calculating matrix elements rely on the Wigner-Eckart theorem. It is valid for a matrix element $\langle JM|T_{kq}|J'M'\rangle$ where J is an arbitrary momentum quantum number and M the corresponding magnetic quantum number. It states that we can factor out the so called reduced matrix element $(J||T_k||J')$, that is independent of q, M, and M', from the matrix element:

$$\langle JM|T_{kq}|J'M'\rangle = (-1)^{J-M}(J||T_k||J')\begin{pmatrix} J & k & J' \\ -M & q & M' \end{pmatrix}. \tag{B.1}$$

Here, the last term is the Wigner 3-j symbol. By calculating the matrix element for $q = 0$ and $M = M'$ directly, i.e. without using the formula, and comparing the result with the right hand side of B.1, we can obtain the value of the reduced matrix element. This will work for momentum and dipole operators, for example.

Momentum operator

We can relate the momentum operators $\hat{J}_x$, $\hat{J}_y$, and $\hat{J}_z$ to spherical tensors $\hat{J}_{1q}$.

$$J_{1\pm1} = \mp\frac{1}{\sqrt{2}}(\hat{J}_x \pm \mathrm{i}\hat{J}_y) = \mp\frac{\hat{J}_\pm}{\sqrt{2}} \tag{B.2}$$

$$J_{10} = \hat{J}_z \tag{B.3}$$

Their reduced matrix element is

$$(J||J||J') = \hbar\sqrt{J(J+1)(2J+1)}o_R\ \delta_{JJ'}, \tag{B.4}$$

where o_R[1] is the overlap between the radial parts of the atomic wave functions $R_{n,l,j}$[2]

$$o_R = \int_0^\infty \mathrm{d}r\ R^*_{n,l,j}(r) R_{n',l',j'}(r). \tag{B.5}$$

Electric dipole operator

Likewise, we can proceed with the electric dipole operator $\hat{\boldsymbol{d}} = e\hat{\boldsymbol{r}}$. By changing to the spherical basis, its components $\hat{d}_x$, $\hat{d}_y$, and $\hat{d}_z$ can be related to spherical tensors d_{1q} [34]:

$$d_{1\pm1} = \mp\frac{1}{\sqrt{2}}(\hat{d}_x \pm \mathrm{i}\hat{d}_y) = \sqrt{\frac{4\pi}{3}}|\hat{\boldsymbol{d}}|Y_1^{\pm1}, \tag{B.6}$$

$$d_{10} = \hat{d}_z = \sqrt{\frac{4\pi}{3}}|\hat{\boldsymbol{d}}|Y_1^0. \tag{B.7}$$

Now, the reduced matrix element is given by

$$(l||d||l') = (-1)^l\sqrt{(2l+1)(2l'+1)}\begin{pmatrix} l & 1 & l' \\ 0 & 0 & 0 \end{pmatrix} d_R = (-1)^{l+l_\mathrm{max}}\sqrt{l_\mathrm{max}} d_R\ \delta_{l,l'\pm1}, \tag{B.8}$$

where d_R is the radial part of the dipole matrix element

$$d_R = e\int_0^\infty \mathrm{d}r\ r^3 R^*_{n,l,j}(r) R_{n',l',j'}(r). \tag{B.9}$$

Coupled angular momenta

The Wigner-Eckart theorem also holds for matrix elements $\langle J_1 J_2 J M|T_{kq}|J_1' J_2' J' M'\rangle$ with a coupled angular momentum $J = J_1 + J_2$ (e.g. the total angular momentum $j = l + s$). Let us assume that T_{kq} commutes with J_2. This leads to $J_2' = J_2$ and we obtain

$$\langle J_1 J_2 J M|T_{kq}|J_1' J_2 J' M'\rangle = (-1)^{J-M}(J_1 J_2 J||T_k||J_1' J_2 J')\begin{pmatrix} J & k & J' \\ -M & q & M' \end{pmatrix}. \tag{B.10}$$

The new reduced matrix element depends on the previously calculated $(J_1||T_k||J_1')$ via

$$(J_1 J_2 J||T_k||J_1' J_2 J') = (-1)^{J_1+J_2+J'+k}(J_1||T_k||J_1')\sqrt{(2J+1)(2J'+1)}\begin{Bmatrix} J_1 & J & J_2 \\ J' & J_1' & k \end{Bmatrix}. \tag{B.11}$$

The last term is the Wigner 6-j symbol. If T_{kq} commutes with J_1, we have

$$(J_1 J_2 J||T_k||J_1 J_2' J') = (-1)^{J_1+J_2'+J+k}(J_2||T_k||J_2')\sqrt{(2J+1)(2J'+1)}\begin{Bmatrix} J_2 & J & J_1 \\ J' & J_2' & k \end{Bmatrix}. \tag{B.12}$$

---

[1] We can split of o_R since wave functions of hydrogen-like atoms detach into an angular and radial part.

[2] $R_{n,l,j}$ can be determined using Numerov's method. This calculation was performed by Sebastian Hofferberth (5th Institute of Physics, University of Stuttgart). He kindly provided us with the results.

C. Zeeman effect

Zeeman effect is called the influence of an external magnetic field on the atomic energy levels.

It can be calculated starting with a classical magnetic dipole with dipole moment $\boldsymbol{\mu}$. Its energy in a magnetic field of strength $\boldsymbol{B}$ [35] is given by

$$V_{\text{Zeeman}} = -\boldsymbol{\mu} \cdot \boldsymbol{B}. \tag{C.1}$$

In quantum mechanics, the dipole moment is replaced by the dipole operator

$$\hat{\boldsymbol{\mu}} = -\tfrac{\mu_{\text{B}}}{\hbar}(g_L \hat{\boldsymbol{L}} + g_S \hat{\boldsymbol{S}}), \tag{C.2}$$

with orbital momentum operator $\hat{\boldsymbol{L}}$, spin momentum operator $\hat{\boldsymbol{S}}$, and the gyromagnetic constants $g_L = 1$ and $g_S \approx 2.0023192$.

Matrix element

We would like to determine the matrix element $\langle nlsjm|\hat{V}_{\text{Zeeman}}|n'l's'j'm'\rangle$ for a magnetic field of arbitrary strength and arbitrary direction. For the work presented in the thesis the magnetic field is weak and points in the direction of the quantization axis, so that simpler and approximative calculations could be done. However, the resulting formulas will be used for numerical calculations and we would like to keep the program for calculating the Zeeman effect as general as possible.

In order to get the Zeeman shift for arbitrary fields, we have to calculate the matrix elements $\langle nlsjm|\hat{\boldsymbol{S}} \cdot \boldsymbol{B}|n'l's'j'm'\rangle$ and $\langle nlsjm|\hat{\boldsymbol{L}} \cdot \boldsymbol{B}|n'l's'j'm'\rangle$. In the following we sketch the calculation of the first expression. The calculation for the other one is done in the same way.

Let us start by expanding the scalar product

$$\begin{aligned}\langle nlsjm|\hat{\boldsymbol{S}} \cdot \boldsymbol{B}|n'l's'j'm'\rangle = \Big(&\langle nlsjm|\hat{S}_x|n'l's'j'm'\rangle B_x + \langle nlsjm|\hat{S}_y|n'l's'j'm'\rangle B_y \\ &+\langle nlsjm|\hat{S}_z|n'l's'j'm'\rangle B_z\Big)\,\delta_{ll'}.\end{aligned} \tag{C.3}$$

We can infer that l has to be equal to l', since $\hat{\boldsymbol{S}}$ commutes with the orbital momentum operator.

To determine the matrix elements of the components of $\hat{\boldsymbol{S}}$, we express them in terms of spherical tensors S_{1q} using equations B.2 and B.3:

$$\hat{S}_x = \frac{1}{\sqrt{2}}(S_{1-1} - S_{1+1}), \tag{C.4}$$

$$\hat{S}_y = \frac{\mathrm{i}}{\sqrt{2}}(S_{1-1} + S_{1+1}), \tag{C.5}$$

$$\hat{S}_z = S_{10}. \tag{C.6}$$

Now, we use formulas B.4, B.5, B.10, and B.12 to compute the matrix element of S_{1q}

$$\begin{aligned}\langle nlsjm|S_{1q}|n'l's'j'm'\rangle = \hbar(-1)^{j-m+s'+l+j+1}\sqrt{(2j+1)(2j'+1)s(s+1)(2s+1)} \\ \times \begin{pmatrix} j & 1 & j' \\ -m & q & m' \end{pmatrix} \begin{Bmatrix} s & j & l \\ j' & s & 1 \end{Bmatrix} \int_0^\infty \mathrm{d}r\ R^*_{n,l,j}(r) R_{n',l',j'}(r)\ \delta_{ll'}\delta_{ss'}.\end{aligned} \tag{C.7}$$

Using B.11, we obtain analogously the matrix element of L_{1q}

$$\begin{aligned}\langle nlsjm|L_{1q}|n'l's'j'm'\rangle = \hbar(-1)^{j-m+s+l+j'+1}\sqrt{(2j+1)(2j'+1)l(l+1)(2l+1)} \\ \times \begin{pmatrix} j & 1 & j' \\ -m & q & m' \end{pmatrix} \begin{Bmatrix} l & j & s \\ j' & l & 1 \end{Bmatrix} \int_0^\infty \mathrm{d}r\ R^*_{n,l,j}(r) R_{n',l',j'}(r)\ \delta_{ll'}\delta_{ss'}.\end{aligned} \tag{C.8}$$

Selection rules

These equations are also useful to derive selection rules. They are given in table C.1.

Selection rule	Reason
$l = l'$	$\delta_{ll'}$
$s = s'$	$\delta_{ss'}$
$m = m' + q$	Wigner 3-j symbol
$j = j', j' \pm 1$	Wigner 3-j symbol

Tab. C.1.: Selection rules for matrix elements of orbital and spin momentum operators.

Zeeman effect for arbitrary magnetic fields

Knowing $\langle nlsjm|\hat{V}_{\text{Zeeman}}|n'l's'j'm'\rangle$, we can choose a basis and write down the Hamiltonian of an atom in a magnetic field $H = H_{\text{free atom}} + \hat{V}_{\text{Zeeman}}$ as a matrix. In order to determine the Zeeman shift of a certain atomic state $|\Psi\rangle$, the basis set should contain $|\Psi\rangle$ itself and all states with quantum numbers similar to the quantum numbers of $|\Psi\rangle$. For $H_{\text{free atom}}$ we use the states' energies relative to the energy of $|\Psi\rangle$. We are interested in hydrogen-like atoms. For them the energies can be calculated similarly to the energy levels of hydrogen. Differences are taken into account by means of quantum defects.

After constructing the Hamiltonian matrix we can diagonalize it. The energy of the eigenstate, whose overlap with $|\Psi\rangle$ is the largest, is an approximation for the Zeeman shift of $|\Psi\rangle$. The basis set is enlarged until this energy has converged.

Zeeman effect for weak magnetic fields

In practice we use the program that implements the general approach mentioned above also for weak fields. However, approximative formulas are important for analytical calculations. Additionally they often provide useful insights into physics. Hence we are interested in them, too. For weak magnetic fields we can find a significant simplification of the formula for the Zeeman effect.

We start with the assumption that the total momentum j is conserved for a weak magnetic field because the spin orbit interaction dominates over the magnetic field. Hence, we have $j = j'$ in addition to $l = l'$ and $s = s'$. Furthermore, if we impose that the magnetic field points in the direction of the quantization axis, only the z-components of the momentum operators matter so that $m = m'$, too. Under these assumptions, the Zeeman shift of the state $|\Psi\rangle = |nlsjm\rangle$ is given by

$$\begin{aligned} V_{\text{Zeeman}} &= \langle nlsjm|\hat{V}_{\text{Zeeman}}|nlsjm\rangle = \frac{\mu_{\text{B}}}{\hbar} B\langle nlsjm|g_L\hat{L}_z + g_S\hat{S}_z|nlsjm\rangle \\ &= \frac{\mu_{\text{B}}}{\hbar} B\left(g_L\langle nlsjm|L_{10}|nlsjm\rangle + g_S\langle nlsjm|S_{10}|nlsjm\rangle\right). \end{aligned} \tag{C.9}$$

The matrix elements of the spherical tensors are given by equation C.8 and C.9. Using a computer algebra system like Mathematica we can evaluate them and obtain

$$V_{\text{Zeeman}} = \mu_{\text{B}} g_J m B, \tag{C.10}$$

where

$$g_J = g_L\frac{j(j+1) - s(s+1) + l(l+1)}{2j(j+1)} + g_S\frac{j(j+1) - l(l+1) + s(s+1)}{2j(j+1)} \tag{C.11}$$

is the Landé g-factor.

This is the well known result for weak magnetic fields derived from the universal formulas for arbitrary magnetic fields. If we just had been interested in obtaining this result, we would have rewritten the matrix element of $g_L\hat{L}_z + g_S\hat{S}_z$ as a matrix element of $\hat{J}_z$. This simplified calculation can be found in [33].

D. Stark effect

The effect of an external electric field on atomic energy levels is called Stark effect.

It originates from the interaction of an electric dipole moment $\boldsymbol{d}$ with an an electric field of strength $\boldsymbol{E}$. Classically, the interaction leads to the energy [35]

$$V_{\text{Stark}} = -\boldsymbol{d} \cdot \boldsymbol{E}. \tag{D.1}$$

In quantum mechanics, the dipole moment is replaced by the dipole operator

$$\hat{\boldsymbol{d}} = e\hat{\boldsymbol{r}}. \tag{D.2}$$

Matrix element

In order to determine the matrix element $\langle nlsjm|\hat{V}_{\text{Stark}}|n'l's'j'm'\rangle$, we have to evaluate

$$\begin{aligned}\langle nlsjm|\hat{\boldsymbol{d}} \cdot \boldsymbol{E}|n'l's'j'm'\rangle = \Big(&\langle nlsjm|\hat{d}_x|n'l's'j'm'\rangle E_x + \langle nlsjm|\hat{d}_y|n'l's'j'm'\rangle E_y \\ &+\langle nlsjm|\hat{d}_z|n'l's'j'm'\rangle E_z\Big)\, \delta_{ss'}.\end{aligned} \tag{D.3}$$

It has to be $s = s'$ since the dipole operator does not affect the spin.

The evaluation can be done by expressing the components of $\hat{\boldsymbol{d}}$ in terms of spherical tensors d_{1q} using equations B.6 and B.7.

$$\hat{d}_x = \frac{1}{\sqrt{2}}(d_{1-1} - d_{1+1}) \tag{D.4}$$

$$\hat{d}_y = \frac{\mathrm{i}}{\sqrt{2}}(d_{1-1} + d_{1+1}) \tag{D.5}$$

$$\hat{d}_z = d_{10} \tag{D.6}$$

Combining equations B.8, B.9, B.10, and B.11 gives us

$$\begin{aligned}\langle nlsjm|d_{1q}|n'l's'j'm'\rangle &= e(-1)^{j-m+s+j'+1+l_{\max}}\sqrt{(2j+1)(2j'+1)l_{\max}} \\ &\times \begin{pmatrix} j & 1 & j' \\ -m & q & m' \end{pmatrix} \begin{Bmatrix} l & j & s \\ j' & l' & 1 \end{Bmatrix} \int_0^\infty \mathrm{d}r\, r^3 R^*_{n,l,j}(r) R_{n',l',j'}(r)\, \delta_{l,l'\pm 1}\delta_{ss'}.\end{aligned} \tag{D.7}$$

This formula makes it possible to calculate the matrix element of the Stark effect $\langle nlsjm|\hat{V}_{\text{Stark}}|n'l's'j'm'\rangle$.

Selection rules

Furthermore it tells us the selection rules that can be found in table D.1.

Selection rule	Reason
$l = l' \pm 1$	$\delta_{l,l'\pm 1}$
$s = s'$	$\delta_{ss'}$
$m = m' + q$	Wigner 3-j symbol
$j = j', j' \pm 1$	Wigner 3-j symbol

Tab. D.1.: Selection rules for dipole matrix elements.

Calculating the Stark effect

Being able to calculate $\langle nlsjm|\hat{V}_{\text{Stark}}|n'l's'j'm'\rangle$ allows us to determine the Stark shift. The linear Stark effect for degenerate states can be computed by first order perturbation theory. For stronger fields the quadratic Stark effect becomes important. It can be calculated by means of second order perturbation theory. However, the perturbative treatment fails as soon as the electric field is strong enough to cause avoided crossings.

A method that also works for such cases is to write down the Hamiltonian $H = H_{\text{free atom}} + \hat{V}_{\text{Stark}}$ in a large enough basis and to diagonalize it — just like for the Zeeman effect, see appendix C. This will give us the Stark shifted energy levels. The approach is computationally more costly than perturbation theory due to the matrix diagonalization.

E. Dipolar interaction

In this section we would like to derive the dipolar interaction operator. In order to do so we first think of an atom as a classical charge distribution. The potential outside the charge distribution can be expressed as a multipole expansion [35]

$$\Phi(\boldsymbol{r}) = \frac{1}{4\pi\epsilon_0}\left[\frac{q}{|\boldsymbol{r}|} + \frac{\boldsymbol{d}\cdot\boldsymbol{r}}{|\boldsymbol{r}|^3} + \frac{1}{2}\sum_{ij} Q_{ij}\frac{r_i r_j}{|\boldsymbol{r}|^5} + ...\right]. \tag{E.1}$$

The dominant term is the dipole term $\Phi_{\text{dipole}} = \frac{\boldsymbol{d}\cdot\boldsymbol{r}}{4\pi\epsilon_0|\boldsymbol{r}|^3}$ since we have neutral atoms. Here, $\boldsymbol{d}$ is the electric dipole moment (in other fields of physics it might be more common to use $\boldsymbol{p}$ as symbol for it). The field of a dipole positioned at $\boldsymbol{r} = 0$ is

$$\boldsymbol{E}_{\text{Dipole}}(\boldsymbol{r}) = -\nabla\Phi_{\text{Dipole}} = \frac{3\boldsymbol{n}(\boldsymbol{n}\cdot\boldsymbol{d}) - \boldsymbol{d}}{4\pi\epsilon_0|\boldsymbol{r}|^3}, \tag{E.2}$$

where $\boldsymbol{n} = \frac{\boldsymbol{r}}{|\boldsymbol{r}|}$ is the unit vector pointing from the position of the dipole to the point in space at which we would like to calculate the field.

We now place a second dipole at position $\boldsymbol{r}$. Then the electrostatic energy of the system, i.e. the dipole-dipole interaction energy, is given by

$$V_{\text{dd}} = -\boldsymbol{d}_2\cdot\boldsymbol{E}_{\text{Dipole 1}} = \frac{\boldsymbol{d}_1\boldsymbol{d}_2 - 3(\boldsymbol{n}\cdot\boldsymbol{d}_1)(\boldsymbol{n}\cdot\boldsymbol{d}_2)}{4\pi\epsilon_0 R^3}. \tag{E.3}$$

Here, $R = |\boldsymbol{r}|$ is the distance between the dipoles. $\boldsymbol{n}$ is a unit vector pointing from the first dipole to the second one, i.e. along the interatomic axis.

The quantum mechanical version of this expression is obtained by replacing the dipole moment with the dipole operator $\hat{\boldsymbol{d}} = e\hat{\boldsymbol{r}}$. Hereby we obtain the dipolar interaction operator $\hat{V}_{\text{dd}}$.

We make use of equations B.6 and B.7 to write the components of the dipole operator as sum of spherical tensors $d_{j,1q}$, where j denotes which dipole is considered. In the following we use $d_j^{\pm}$ and d_j^0 as abbreviations for $d_{j,1\pm1}$ and $d_{j,10}$. We have

$$\hat{d}_j^x = \frac{1}{\sqrt{2}}(d_j^- - d_j^+), \tag{E.4}$$

$$\hat{d}_j^y = \frac{\mathrm{i}}{\sqrt{2}}(d_j^- + d_j^+), \tag{E.5}$$

$$\hat{d}_j^z = d_j^0. \tag{E.6}$$

This allows us to write the dipolar inteaction operator in terms of $d_j^{\pm}$ and d_j^0:

$$\hat{V}_{12}^{\mathrm{dd}} = \frac{1}{4\pi\epsilon_0 R^3}\left[d_1^0 d_2^0 - d_1^+ d_2^- - d_1^- d_2^+ \right. \tag{E.7}$$

$$-\frac{3}{2}\left(\sqrt{2}n_z d_1^0 + (\mathrm{i}n_y - n_x)d_1^+ + (\mathrm{i}n_y + n_x)d_1^-\right)$$

$$\left.\times\left(\sqrt{2}n_z d_2^0 + (\mathrm{i}n_y - n_x)d_2^+ + (\mathrm{i}n_y + n_x)d_2^-\right)\right]. \tag{E.8}$$

The matrix elements of the spherical tensors and hence the matrix elements of the interaction operator can be calculated with equation D.7.

Interatomic axis perpendicular to quantization axis

In this thesis we investigate atoms in a lattice with a magnetic field perpendicular to the lattice plane. Since we choose the quantization axis to be parallel to the magnetic field, we are interested in the case that the interatomic axis is perpendicular to the quantization axis (see figure E.1). Then, the unit vector that points from dipole one to dipole two can be parametrized as

$$\boldsymbol{n} = \begin{pmatrix} \cos\phi_{12} \\ \sin\phi_{12} \\ 0 \end{pmatrix}, \tag{E.9}$$

where ϕ_{12} is the polar angle of the vector $\boldsymbol{r}_2 - \boldsymbol{r}_1$. This results in the following expression for the dipolar interaction operator

$$\hat{V}_{12}^{\mathrm{dd}} = \frac{1}{4\pi\epsilon_0 R^3}\left[d_1^0 d_2^0 - d_1^+ d_2^- - d_1^- d_2^+ \right. \tag{E.10}$$

$$\left. -\frac{3}{2}\left(-\mathrm{e}^{-\mathrm{i}\phi_{12}} d_1^+ + \mathrm{e}^{\mathrm{i}\phi_{12}} d_1^-\right)\left(-\mathrm{e}^{-\mathrm{i}\phi_{12}} d_2^+ + \mathrm{e}^{\mathrm{i}\phi_{12}} d_2^-\right)\right]$$

$$= \frac{1}{4\pi\epsilon_0 R^3}\left[d_1^0 d_2^0 + \frac{1}{2}\left(d_1^+ d_2^- + d_1^- d_2^+\right) - \frac{3}{2}\left(d_1^- d_2^- \mathrm{e}^{2\mathrm{i}\phi_{12}} + d_1^+ d_2^+ \mathrm{e}^{-2\mathrm{i}\phi_{12}}\right)\right]. \tag{E.11}$$

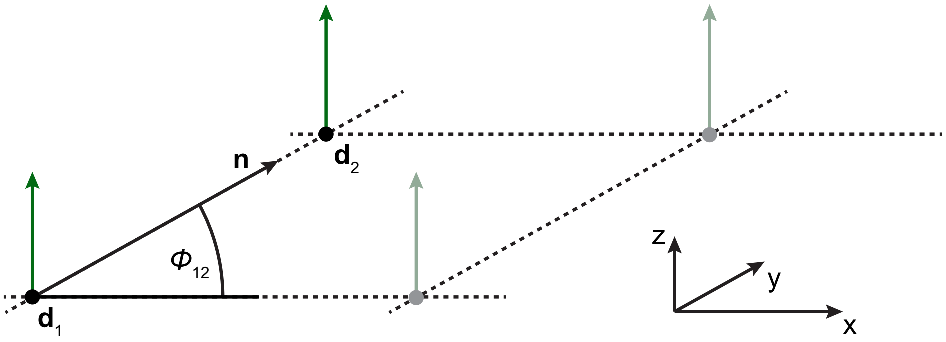

Fig. E.1.: Visualization of the geometrical conditions that occur in a lattice of atoms where the quantization axis (shown in green) is perpendicular to the lattice plane.

F. High performance computing with Python

We can write sophisticated software in Python [36] comparatively quick and easy for various reasons: It is designed for good readability and has a great documentation. It is open-source, cross-platform, and there are powerful programming libraries that can be easily installed. Normally, one needs much less lines of codes to write software in Python than in a more low-level programming language like C.

Some of these advantages are gained by a loss of performance: Being a scripting language with a dynamic type system, a lot of information can be only determined at runtime. There is no compiler that does optimizations in advance. Hence, scripting languages like Python are generally considered a bad choice for high performance computing. However, this is not completely true. External libraries can be often used to circumvent the performance issues. Another possibility would be to program in Cython [37] that brings type declaration and compiler optimizations to Python. But normally, the use of external libraries is sufficient for our purposes.

In the following we present some handy libraries for Python 3 and general concepts that are useful for high performance computing.

F.1. Vectorization with NumPy

The key idea is to let libraries do the time consuming work. For this purpose, the Python library NumPy [38, 39] is a great starting point. It uses BLAS and LAPACK for fast linear algebra operations. Further acceleration can be obtained with specialized libraries like Numexpr [40].

To demonstrate the power of NumPy, we benchmark[1] several ways of calculating the sum $\sum_{j=1}^{n} \sqrt{j}$ for various values of n:

```
#!/usr/bin/env python3

import numpy as np
import numexpr as ne

```

---

[1] We perform the benchmark on a MacBook Pro with a 2.5 GHz Intel i7-4870HQ processor.

```
ne.set_num_threads(1)

# (1) Calculation using a for loop
def fct1(n):
    result = 0
    for j in range(1,n+1):
        result += j**0.5

# (2) Calculation using NumPy’s internal rutines
def fct2(n):
    vec = np.arange(1,n+1)
    result = np.sum(vec**0.5) # array**0.5 is the same as np.sqrt(array)

# (3) Calculation using NumPy in combination with Numexpr
def fct3(n):
    vec = np.arange(1,n+1)
    result = ne.evaluate(’vec**0.5’).sum()

# Benchmarking
if __name__ == ’__main__’:
    import timeit

    for fct in [’fct1’,’fct2’, ’fct3’]:
        stp =’from __main__ import ’+fct
        print(timeit.timeit(fct+’(1000000)’, setup=stp, number=10)/10)
```

The slowest approach is the calculation with a for loop, see figure F.1.

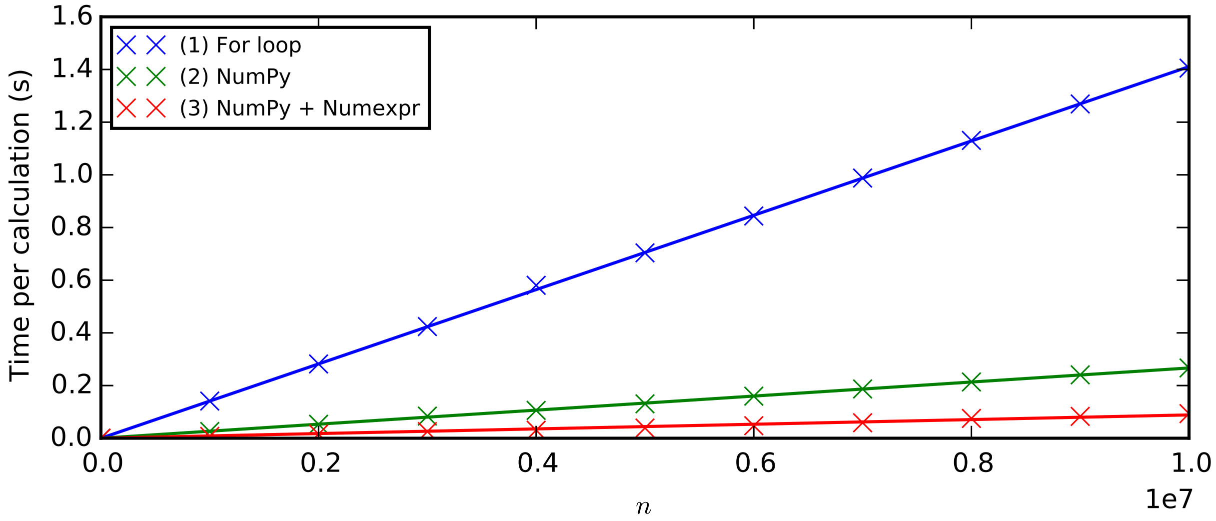

Fig. F.1.: Time consumption of the calculation of $\sum_{j=1}^{n} \sqrt{j}$ as a function of n. The computation with a for loop takes much longer than vectorized calculations. NumPy combined with Numexpr performs the fastest.

This observation is consistent with our experience. In scripting languages like Python, it is in general a good idea to avoid loops that repeat a lot of times. For the approaches based on NumPy, we vectorize our calculation[2]: Instead of looping over all numbers up to n, we let NumPy construct an integer array. Then, we perform operations on this array to get the result. The strong speed-up through Numexpr originates from the use of Intel's Vector Math Library.

Of course, vectorization is not always as easy as in this example. In more complicated cases NumPy's excellent array indexing mechanisms might help [38]. In practice, the "newaxis" keyword (one can also use "None" instead) turns out to be especially useful. Since it is not so well-known, we explain it here. The "newaxis" keyword modifies the shape of an array by inserting a dimension equal to one:

```
#!/usr/bin/env python3

import numpy as np

arr1 = np.random.rand(4,6,2) # random array of shape (4,6,2)
arr2 = arr[:,np.newaxis,:,:] # array brought in to the shape (4,1,6,2)
```

To understand, why this is helpful, we have to comprehend how NumPy handles the element-wise multiplication of two arrays. In general, both arrays need to be of the same shape to allow this operation, i.e. they must match in all their dimensions. There is a special case where NumPy internally corrects the shape of the arrays: It adjusts dimensions that are equal to one and thus also all dimensions created with "newaxis". For example, an array of shape $(5, 8, 7, 1)$ can be multiplied with an array of shape $(5, 8, 7, 10)$. In order to make this possible, NumPy repeats the first array ten times along the last axis.

Knowing this, we can use the keyword "newaxis" to perform operations such as tensor products and matrix multiplications on high dimensional arrays. As an example, let us define the matrix multiplication for vectors of matrices:

```
#!/usr/bin/env python3

import numpy as np

# vecMatA of shape (number of matrices = 1e5, rows = 10, columns = 15)
vecMatA = np.random.rand(1e5,10,15)

# vecMatB of shape (number of matrices = 1e5, rows = 15, columns = 20)
vecMatB = np.random.rand(1e5,15,20)

# vecMatA*vecMatB of shape (number of matrices = 1e5, rows = 10, columns = 20)
vecMatC = np.sum(vecMatA[:,:,:,np.newaxis]*vecMatB[:,np.newaxis,:,:], axis=2)
```

---

[2] One should keep an eye on the memory consumption since vectorization can lead to huge arrays.

Formally, this calculation is equivalent to a loop over the vectors of matrices where we apply the standard matrix product consecutively. However, as we have demonstrated before, this approach would be much slower than our fully vectorized calculation.

F.2. Parallelization and load balancing with MPI4Py

As an example, the calculation of phase diagrams is well suited for parallelization. Here, similar calculations have to be performed for different sets of parameters. Since all calculations are independent of each other, processes performing calculations need no communication amongst each other. Such "perfectly parallel" problems should be parallelized before one starts thinking about the parallelization of calculations where a lot of communication is needed.

To make optimal use of all processors, it is usually recommended to start as many processes as cores. Now, the question is how to distribute the work among the processes. One possibility would be to assign pieces of work to processes at the start of the program. However, if a process has done its work, it will then remain unemployed until the end of the program. Hence, it is better to dynamically assign work. This assignment is done by a special process called "master". It checks the other processes, called "slaves", and gives them work in case they are not busy. Such a load balancing system is often implemented via MPI, the Message Passing Interface. A Python library that provides MPI is MPI4Py [41]. A basic implementation of load balancing is given below:

```
#!/usr/bin/env python3

from mpi4py import MPI

WORKTAG = 0
DIETAG = 1

status = MPI.Status()
comm = MPI.COMM_WORLD
rank = comm.Get_rank()

# If rank == 0, this instance the master
if rank == 0:
    numProcesses = comm.Get_size()
    numWorking = 1

    arrWork = range(1000)
    arrResult = []

    for work in arrWork: # distribute work and receive results
        if numWorking < numProcesses:
            destination = numWorking
```

```
            numWorking += 1
        else:
            arrResult.append(comm.recv(source=MPI.ANY_SOURCE, status=status))
            destination = status.Get_source()

        comm.send(obj=work, dest=destination, tag=WORKTAG)

    for j in range(1,numWorking): # collect until now unreceived results
        arrResult.append(comm.recv(source=MPI.ANY_SOURCE, status=status))

    for j in range(1,numProcesses): # terminate all slaves
        comm.send(obj=None, dest=j, tag=DIETAG)

    print(arrResult)

# If rank != 0, this instance is a slave
else:
    while True:
        work = comm.recv(source=0, tag=MPI.ANY_TAG, status=status)
        if status.Get_tag() == DIETAG: # exit slave
            break
        if status.Get_tag() == WORKTAG: # do work
            result = work**0.5
            comm.send(obj=result, dest=0)
```

The script can be started via “mpiexec python3 scriptname.py”.

F.3. Computer monitoring with Paramiko

We would like to keep track of the system load while testing new programs — especially, if we wish to do high performance computing and rely on the optimal usage of available resources. For example, it is important to recognize, if a program runs out of memory.

If a program is executed on many computers in parallel, it is a hard job to check the system load on each of them manually. Hence, we automatize this task using Python scripts. The SSH library Paramiko is very helpful for this [42]. As an example we show a script that can be used to get the memory usage of all accessible computers in our network:

```
#!/usr/bin/env python3

from multiprocessing.pool import ThreadPool
from paramiko import SSHClient, AutoAddPolicy

user = "sebastian"
proxyname = "holle"
proxyport = 3231 # used for SSH tunnel
```

```
sshport = 22

class SSHConnection: # script relies on key based SSH authentication
    def __init__(self, *args, **kwargs):
        self.args = args
        self.kwargs = kwargs
    def __enter__(self):
        self.ssh = SSHClient()
        self.ssh.load_system_host_keys()
        self.ssh.set_missing_host_key_policy(AutoAddPolicy())
        self.ssh.connect(*self.args, **self.kwargs)
        return self.ssh
    def __exit__(self, type, value, traceback):
        self.ssh.close()

# Connect to SSH tunnel proxy
with SSHConnection(proxyname, username=user, timeout=2) as tunnel:
    transport = tunnel.get_transport()

    # Generate possible hostnames
    hostnames = [’129.69.66.{}’.format(n) for n in range(256)]
    hostnames.append([’10.0.0.{}’.format(n) for n in range(256)])

    def worker(hostname):
        try:
            # Connect to hosts via the proxy
            openchannel = lambda : transport.open_channel("direct-tcpip", \
                (hostname, sshport), (’127.0.0.1’, proxyport))
            res = ThreadPool(1).apply_async(openchannel)
            channel = res.get(timeout=2)
            with SSHConnection(’127.0.0.1’, username=user, port=proxyport, \
                sock=channel, timeout=2) as ssh:
                stdin, stdout, stderr = ssh.exec_command("free -k | awk ’/
                    buffers\/cache/ {print $3}’")
                if stdout.channel.recv_exit_status() != 0: raise
                usedmemory = int(stdout.read())*1e-6 # in Gigabytes
                return [hostname,usedmemory]
        except:
            return None

    pool = ThreadPool(processes=len(hostnames))
    results = pool.map(worker, hostnames)
```

A nice property of the script is, that it is very fast since all computers are checked in parallel. Likewise, we can obtain the CPU load or system specifications of remote computers. Such scripts can be used to kill frozen programs or zombie processes, too.

List of tables

List of figures

Bibliography

[1] D. C. Tsui, H. L. Stormer, and A. C. Gossard, “Two-Dimensional Magnetotransport in the Extreme Quantum Limit,” *Physical Review Letters*, vol. 48, pp. 1559–1562, May 1982.

[2] R. B. Laughlin, “Anomalous Quantum Hall Effect: An Incompressible Quantum Fluid with Fractionally Charged Excitations,” *Physical Review Letters*, vol. 50, pp. 1395–1398, May 1983.

[3] M. Z. Hasan and C. L. Kane, “Colloquium : Topological insulators,” *Reviews of Modern Physics*, vol. 82, pp. 3045–3067, Nov. 2010.

[4] X.-L. Qi and S.-C. Zhang, “Topological insulators and superconductors,” *Reviews of Modern Physics*, vol. 83, pp. 1057–1110, Oct. 2011.

[5] K. V. Klitzing, G. Dorda, and M. Pepper, “New Method for High-Accuracy Determination of the Fine-Structure Constant Based on Quantized Hall Resistance,” *Physical Review Letters*, vol. 45, pp. 494–497, Aug. 1980.

[6] D. Peter, N. Y. Yao, N. Lang, S. D. Huber, M. D. Lukin, and H. P. Büchler, “Topological bands with a Chern number C=2 by dipolar exchange interactions,” *Physical Review A*, vol. 91, p. 053617, May 2015.

[7] C.-K. Chiu, J. C. Y. Teo, A. P. Schnyder, and S. Ryu, “Classification of topological quantum matter with symmetries,” *arXiv:1505.03535 [cond-mat.mes-hall]*, 2015.

[8] F. D. M. Haldane, “Model for a quantum hall effect without landau levels: Condensed-matter realization of the "parity anomaly",” *Physical Review Letters*, vol. 61, no. 18, pp. 2015–2018, 1988.

[9] M. Levin and A. Stern, “Fractional Topological Insulators,” *Physical Review Letters*, vol. 103, p. 196803, Nov. 2009.

[10] B. Jeckelmann and B. Jeanneret, “The quantum Hall effect as an electrical resistance standard,” *Reports on Progress in Physics*, vol. 64, pp. 1603–1655, Dec. 2001.

[11] C. Nayak, S. H. Simon, A. Stern, M. Freedman, and S. Das Sarma, “Non-Abelian anyons and topological quantum computation,” *Reviews of Modern Physics*, vol. 80, pp. 1083–1159, Sept. 2008.

[12] P. Hauke, O. Tieleman, A. Celi, C. Ölschläger, J. Simonet, J. Struck, M. Weinberg, P. Windpassinger, K. Sengstock, M. Lewenstein, and A. Eckardt, “Non-Abelian Gauge Fields and Topological Insulators in Shaken Optical Lattices,” *Physical Review Letters*, vol. 109, p. 145301, Oct. 2012.

[13] G. Jotzu, M. Messer, R. Desbuquois, M. Lebrat, T. Uehlinger, D. Greif, and T. Esslinger, “Experimental realization of the topological Haldane model with ultracold fermions,” *Nature*, vol. 515, pp. 237–240, Nov. 2014.

[14] H. Miyake, G. a. Siviloglou, C. J. Kennedy, W. C. Burton, and W. Ketterle, “Realizing the Harper Hamiltonian with Laser-Assisted Tunneling in Optical Lattices,” *Physical Review Letters*, vol. 111, p. 185302, Oct. 2013.

[15] M. Mancini, G. Pagano, G. Cappellini, L. Livi, M. Rider, J. Catani, C. Sias, P. Zoller, M. Inguscio, M. Dalmonte, and L. Fallani, “Observation of chiral edge states with neutral fermions in synthetic Hall ribbons,” *Science*, vol. 349, pp. 1510–1513, Sept. 2015.

[16] B. K. Stuhl, H.-I. Lu, L. M. Aycock, D. Genkina, and I. B. Spielman, “Visualizing edge states with an atomic Bose gas in the quantum Hall regime,” *Science*, vol. 349, pp. 1514–1518, Sept. 2015.

[17] S. V. Syzranov, M. L. Wall, V. Gurarie, and A. M. Rey, “Spin-orbital dynamics in a system of polar molecules,” *Nature Communications*, vol. 5, p. 5391, Nov. 2014.

[18] B. Bernevig and T. Hughes, *Topological Insulators and Topological Superconductors*. Princeton University Press, 2013.

[19] G. M. Graf and M. Porta, “Bulk-Edge Correspondence for Two-Dimensional Topological Insulators,” *Communications in Mathematical Physics*, vol. 324, pp. 851–895, Dec. 2013.

[20] Y. Hatsugai, “Chern number and edge states in the integer quantum Hall effect,” *Physical Review Letters*, vol. 71, pp. 3697–3700, Nov. 1993.

[21] N. Ashcroft and D. Mermin, *Festkörperphysik*. Oldenbourg Wissenschaftsverlag, 2012.

[22] H. Labuhn, D. Barredo, S. Ravets, S. de Léséleuc, T. Macrì, T. Lahaye, and A. Browaeys, “A highly-tunable quantum simulator of spin systems using two-dimensional arrays of single rydberg atoms,” *arXiv:1509.04543 [cond-mat.quant-gas]*, 2015.

[23] T. Neupert, L. Santos, C. Chamon, and C. Mudry, “Fractional quantum hall states at zero magnetic field,” *Physical review letters*, vol. 106, no. 23, p. 236804, 2011.

[24] D. Applegate, R. Bixby, V. Chvátal, and W. Cook, *The Traveling Salesman Problem: A Computational Study*. Princeton Series in Applied Mathematics, Princeton University Press, 2 ed., 2011.

[25] M. Dorigo, M. Birattari, and T. Stutzle, “Ant colony optimization,” *IEEE Computational Intelligence Magazine*, vol. 1, pp. 28–39, Nov. 2006.

[26] F. Nogrette, H. Labuhn, S. Ravets, D. Barredo, L. Béguin, A. Vernier, T. Lahaye, and A. Browaeys, “Single-Atom Trapping in Holographic 2D Arrays of Microtraps with Arbitrary Geometries,” *Physical Review X*, vol. 4, p. 021034, May 2014.

[27] A. Schwettmann, J. Crawford, K. R. Overstreet, and J. P. Shaffer, “Cold Cs

Rydberg-gas interactions," *Physical Review A*, vol. 74, p. 020701, Aug. 2006.

[28] J. Honer, H. Weimer, T. Pfau, and H. P. Büchler, "Collective Many-Body Interaction in Rydberg Dressed Atoms," *Physical Review Letters*, vol. 105, p. 160404, Oct. 2010.

[29] P. Bienias, S. Choi, O. Firstenberg, M. F. Maghrebi, M. Gullans, M. D. Lukin, a. V. Gorshkov, and H. P. Büchler, "Scattering resonances and bound states for strongly interacting Rydberg polaritons," *Physical Review A*, vol. 90, no. 5, p. 053804, 2014.

[30] M. Abramowitz, I. Stegun, and N. Sfetcu, *Handbook of Mathematical Functions: With Formulas, Graphs, and Mathematical Tables.* Nicolae Sfetcu, 2014.

[31] G. Drake, *Springer Handbook of Atomic, Molecular, and Optical Physics.* Springer, 2005.

[32] Wikipedia, "Atomic units." `https://en.wikipedia.org/w/index.php?title=Atomic_units&oldid=663497800`, 2015. [Accessed 9-October-2015].

[33] I. Sobelman, *Atomic Spectra and Radiative Transitions.* Springer Series on Atomic, Optical, and Plasma Physics, Springer, 2 ed., 1996.

[34] A. Urvoy, "Set-up of a laser system for precision spectroscopy of highly excited caesium atoms," Diplomarbeit, University of Stuttgart, 5th Institute of Physics, 2011.

[35] J. Jackson, *Classical Electrodynamics.* Wiley, 3 ed., 1998.

[36] Python Software Foundation, Python programming language, `http://www.python.org`. [Accessed 1-November-2015].

[37] R. Bradshaw, S. Behnel, D. S. Seljebotn, G. Ewing, et al., The Cython compiler, `http://cython.org`. [Accessed 1-November-2015].

[38] T. E. Oliphant, "Python for Scientific Computing," *Computing in Science & Engineering*, vol. 9, no. 3, pp. 10–20, 2007.

[39] NumPy developers, NumPy Python package, `http://www.numpy.org`. [Accessed 1-November-2015].

[40] Numexpr developers, Fast numerical expression evaluator for NumPy, `http://github.com/pydata/numexpr`. [Accessed 1-November-2015].

[41] L. Dalcín, R. Paz, and M. Storti, "MPI for Python," *Journal of Parallel and Distributed Computing*, vol. 65, pp. 1108–1115, Sept. 2005.

[42] Paramiko developers, A Python implementation of SSHv2, `http://www.paramiko.org`. [Accessed 1-November-2015].

Acknowledgements

I would like to use this last page to thank persons who supported me during the time of my master thesis.

First of all, I would like to give thanks to Hans Peter Büchler and David Peter for their great supervision. Hans Peter, thank you for all the inspiring discussions and stimulating input as well as for providing me the opportunity to visit interesting conferences already in an early stage of my thesis. David, thank you for all the support and great ideas concerning physics, the english language, as well as coding. I have learned a lot from you.

I would like to express my thanks to Thierry Lahaye and Antoine Browaeys with whom we have a great collaboration. They offered essential input for the experimental proposal and told us what might be experimentally feasible. In addition, I would like to thank Sebastian Hofferberth from whom I have learned much about interaction of Rydberg atoms during my time as a HiWi in his work group. He kindly provided us his database of dipole matrix elements. Moreover, I would like to give thanks to Jörg Main who have taken time for discussing the results of my work in detail.

Further thanks goes to the members of our institute — in particular to Przemek Bienias, Friedemann Aust, Kai Guther, and Nicolai Lang. Thank you for all the interesting discussions about topics related to my thesis as well as about physics and nature in general.

In addition I would like to thank my friends for awesome conversations, activities, and hiking tours that served as a fantastic balance to the work on my thesis.

Last but not least I would like to give special thanks to my family and Nina for their great support.